JET-R(94)07

Lower Hybrid Heating and Current Drive in ITER: Operation Scenarios and Outline System Design

A Kaye, D Moreau[3], F X Söldner,
F. Engelmann[1], C Gormezano, B Lloyd[2], F Santini[4],
G Tonon[3], J G Wegrowe[1],
Y Baranov, V P Bhatnagar, M Goniche[3], , G T A Huysmans,
X Litaudon[3], M R O'Brien[2], V V Parail, G Rey[3], E Springmann,
A Taroni, R Walton, C D Warrick[2].

JET Joint Undertaking, Abingdon, Oxfordshire, OX14 3EA, UK.
[1] NET, Garching, Germany.
[2] AEA, Culham Laboratory, Abingdon, Oxfordshire, OX14 3DB, UK.
[3] CEA, Cadarache, France.
[4] ENEA, Frascati, Italy.

This report has been prepared by the members and the permanent participants of the European Coordinating Committee on Lower Hybrid Waves (CCHL).

November 1994

OUTLINE

EXECUTIVE SUMMARY

1. LOWER HYBRID WAVES IN ITER

Lower Hybrid Waves (LHW) are considered a valid method of plasma heating and the best demonstrated current drive method. Current drive by LHW possesses the unique feature, as compared to the other methods, to retain a good current drive efficiency in plasma regions of low to medium temperature, or in low-ß phases of the discharges. This makes them an essential element to realize the so-called 'advanced steady-state Tokamak scenarios' in which a hollow current density profile (deep shear reversal) - established during the ramp-up of the plasma current - offers the prospects of improved confinement and an MHD-stable route to continuous burn.

This report contains both modelling and design studies of an LHW system for ITER. It aims primarily at the definition of concepts and parameters for steady-state operation using LHW combined with Fast Waves (FW), or other methods of generating a central seed current for high bootstrap current operation. However simulations addressing the use of LHW for current profile control in the high current pulsed operation scenario are also presented. The outline design of a LHW system which covers the needs for both pulsed and steady-state operation is described in detail.

2. MODELLING STUDIES

Recent experimental and theoretical progress has provided a deeper understanding of LHW propagation and power deposition and the predictive simulations presented are based on models now validated on experiments (appendix 1). Various transport codes and transport models have been used to simulate ITER discharges and MHD stability has been investigated in the successive phases of the proposed scenarios. It results that :

i) Steady-state operation at low plasma current appears possible in ITER in the realm of our simulations using a combination of LHW and FW with :

- significant fusion power (1- 1.3 GW),
- $Q \geq 10$ -15,
- high average plasma density (0.8 - 1 x 10^{20} m^{-3}),
- moderate (and thus possibility of control) bootstrap current fraction (≤ 70 %),
- moderate normalized ß,

- acceptable current drive efficiency and confinement according to present criteria.

ii) The discharge evolves through a succession of MHD stable configurations with a deep shear reversal established during the ramp-up phase,

iii) Efficient control of the current profile, and especially sawteeth and m = 1 (possibly m = 2) instabilities can be obtained by LHW in "standard" - high current operation of ITER - as will likely be required for long-pulse operation.

3. SYSTEM DESIGN

The outline design of a launcher for lower Hybrid heating and current drive on ITER is described. This system operates at 5 GHz and couples typically 20 MW through one main horizontal port using a combination of a passive/active waveguide grill with hyperguide and mode convertors feeds to give a structure which combines a robust grill with simple supply networks and good neutron attenuation at the first wall. The proposed design is consistent with the design of other first wall systems in ITER. Whilst the design is based to a large extent on existing technology, a number of areas require further investigation as summarised in section IV.2 in order to ensure the eventual performance of the system.

I. INTRODUCTION.

The objectives of ITER are to demonstrate controlled ignition in pulsed operation with steady-state as an ultimate goal.

To reach the immediate goal of ITER, the heating and Current drive (CD) systems will have to provide not only Heating to ignition, but also burn temperature control and current profile control to act upon sawteeth and MHD activity.

The ultimate objective of testing in ITER steady-state operation imposes operation at a reduced plasma current as compared to the pulsed regime, with a large contribution of bootstrap current, in order for the CD system to provide the rest current with tolerable additional power. Enhanced confinement - required to sustain operation at reduced current - can be expected in discharges with large bootstrap fraction as indicated in recent experiments on DIII-D, JET, JT-60, TFTR and TORE SUPRA.

Recent progress in obtaining enhanced plasma confinement and stability through modifications of the velocity and magnetic shears (central shear reversal), have led to a new reactor concept - the so-called "Advanced Tokamak Concept", which appears promising for relaxing the constraints on the plasma current and thus might have an important cost impact.

While implementing a Lower Hybrid Waves (LHW) system would be useful for standard high current operation in ITER and beneficial in testing "classical" steady-state scenarios, it becomes probably essential for the realization of advanced scenarios owing to the good CD efficiency of LHW at low ß.

For burn conditions at full plasma current (25 MA) in inductive operation, LHW can provide adequate broadening of the current density profile and control the sawtooth activity; this may be necessary to reach a pulse length of 1000s. Moreover, LHCD would offer a possibility for local current profile control in the outermost part of the discharge to control the m=2 mode, and also provide a means for optimizing the start-up conditions and flux consumption through profile control during the current ramp-up.

An MHD stable route to continuous burn with central shear reversal requires - according to recent analyses (see II.1) - to establish hollow current profiles already during the low phase of discharge (and to maintain it during the burn). LHW possess among the envisaged CD methods, the unique property to have a good (and well demonstrated) current drive efficiency in low regions (or phases) of the discharge. Modellings of LHW propagation, power deposition and current drive - now based on an improved understanding of the various physics mechanisms and validated on several experiments - predict penetration of the wave to a zone of moderate ($n_eT_e \leq 10$ to 20 keV 10^{20} m^{-3}) in ITER at 6T ; i.e. a peak of the power deposition around r/a ~ 0.5 to 0.7 during burn and the capability of penetration to the plasma centre during the ramp-up and heating phase. The CD efficiency of LHW is by far the best obtained experimentally (up to 0.4 10^{20} m^{-2} MA/MW).

To implement these advanced scenarios, a combination of LHW and Fast Waves (FW) has been found very attractive and ensures full current drive and profile control. This combination benefits from the characteristics of both methods. The FW current drive efficiency is good in the high temperature plasma centre during burn and adequate to provide the needed seed curent, but decreases rapidly with radius. The resulting very peaked driven current gives an optimal control of the central safety factor, favours a high bootstrap fraction and can be used to adjust it.

FW can also provide central ion heating for efficient and fast burn control (including, if needed, burn initiation - which can be obtained by LHW alone according to the presented simulations).

Section II of this report deals with the modelling of LHW propagation absorption and current drive (II.1) and of operation scenarios described generally in section II.2. Simulation of LHW in the standard high current regime with the JETTO code is described in II.3. Larger emphasis is devoted to steady-state scenarios. For these scenarios the plasma current has to be chosen in a small range around 13MA to meet simultaneously the constraints of significant fusion yield and multiplicator, moderately large bootstrap fraction, high density and moderate normalized . In Section II.4, simulations with JETTO in combination with LHW packages and MHD analyses with the CASTOR code are described in detail - and complementary transport simulations of an advanced scenario with ASTRA, using RLW transport are more briefly reported. This Section also includes a study of feed-back schemes needed to control the q-profile in the various phases of the advanced scenario discharges.

The classical grill launcher now benefits from a large experimental data base, but concerns were expressed about its ability to withstand the conditions of the reactor first wall environment. A number of new concepts are currently under active development to overcome the identified weaknesses. They aim both at increasing the robustness of the plasma coupling structure (active/passive waveguide array ; quasi-optical launcher) and at simplifying the power transmission lines (hyperguide and poloidal mode converter).

While the quasi-optical is a new concept of launcher which deserves grill further theoretical and experimental developments, the active/passive waveguide launcher - adopted for the outline design presented here - is derived from the well developed conventional multijunction grill ; its design uses the same computational tools. The structure alternates active waveguides with short passive waveguides which yields a more robust plasma facing structure, easy to cool actively, and retains essentially the same flexibility and matching ability as the conventional multijunction launcher (though at the cost of a reduced transmitted power density). The plasma facing surface is flush with the blanket elements and ensures electrical continuity for induced toroidal currents at this level. The launcher structure is 60% dense and provides similar neutron shielding as the first wall shield modules.

A considerable simplification of the transmission is achieved by using the hyperguide concept presently under test, in which the RF power is conveyed to the multijunctions by oversized rectangular waveguides. This structure also offers much reduced RF losses and outgasing, as well as an improved pumping.

A complete outline design of a LHW system for ITER able to cover both pulsed operation at full plasma current and steady-state operation is described in **Section III** of this report. It operates at 5 GHz and is based on modules launching 20 to 25 MW per horizontal port. The active/passive waveguide array is flush to the first wall ; it is compatible with the design and constraints of the other in-vessel components (in particular shielding, electrical continuity in the toroidal direction of the first wall, fault pressure rise compatibility in the vessel and in the cryostat). Remote maintenance is accomplished by exchanging the LH-launcher plug from outside the cryostat with the possibility of refurbishing off-line. RF windows are accessible for separate maintenance and are located in a low fluence region to avoid degradation. Mechanical and thermal stress analysis of the main components have been performed, cooling , baking and pumping systems have been dimensionned.

More information on specific issues can be found in **5 appendices** describing respectively the LHW codes and their validation (App.1) ; experiments and feasibility in ITER of LHW coupling at large plasma-launcher distance as proposed in the outline design (App.2); design and optimization calculations of non-conventional element of the LHW system: active/passive array (App.3) ; hyperguide (App. 4) and poloïdal mode converter (App.5).

A final summary collects the main results of the present study which concludes in the feasibility and interest of implementing an LHW system in the ITER device.

II. MODELLING OF OPERATION SCENARIOS.

II.1. Lower Hybrid Waves Propagation, Deposition and Current Drive Studies

For LH application to ITER, parameter studies were carried out with the two ray-tracing/Fokker-Planck codes BARANOV and BANDIT3D (see Appendix 1 for description and validation) in order to optimise the LH wave parameters and to assess the sensitivity of LH current drive schemes to variations of the plasma parameters. Frequencies in the range f=4.5-10GHz were studied, with narrow spectra of a full width of $\Delta N_{||}=0.2$. The peak of the spectrum was varied in the range $N_{||}=1.3\text{-}2.5$. The influence of the poloidal location of the antenna was investigated, with launching from outboard midplane, top, bottom and intermediate positions. Two scenarios in ITER were modelled, the standard case of ITER with 25MA and a steady-state scenario with reduced plasma current of 13.5MA. The main parameters are given in Table II.1.

PARAMETERS	STANDARD CASE (JETTO I0C522)	STEADY STATE (JETTO I00442)
I_p (MA)	25	13.5
I_{bs} (MA)	9	10
I_{LH} (MA)	3.1	2.8
I_{FW} (MA)	0.5	0.7
P_{LH} (MW)	50	50
P_{FW} (MW)	50	50
B (T)	6.2	5.0
q_ψ	3.3	5.0
Z_{eff}	1.4	1.3
n(0) (10^{20} m^{-3})	1.4	1.3
<n> (10^{20} m^{-3})	1.1	1.05
T(0) (keV)	41	32
β_p	1.7	3.8
β_t (%)	4.2	3.1
τ_E (s)	3.6	2.8
β_N	2.9	4.1
H-factor ($\tau_E/\tau_{E,ITER-89}$)	2.1	2.8
P_{fus} (GW)	2.2	1.6

Table II.1. ITER parameters

In the standard case with high density and very flat profiles, LH power is deposited in the peripheral region at r/a ≥ 0.7. The non-inductive current driven by LHCD provides an adequate control of sawteeth and m=1 modes, and of the current profile on the long resistive time scale encountered in ITER.

A possible steady state scenario of ITER has been studied in greater detail with both ray-tracing codes. Remarkable agreement is found between them for most features. The LH power deposition peaks in all cases in a region with the electron pressure in the range $n_eT_e \sim 10^{21}$ keV m^{-3}.

The results of extensive parameter studies with the BANDIT code are summarised in Tables II.2-4. Best penetration is obtained with top launch for both frequencies, 5.5 GHz and 8 GHz, for spectra with the peak at $N_{||} = 2$ (Table II.2). The LH waves are fully absorbed in their first pass through the plasma. The maximum of the deposition profile is located at r/a ~ 0.5 in both cases, with total LH driven currents of similar magnitude. The current drive figure of merit reaches $\eta \sim 0.4 \times 10^{20}$ $AW^{-1}m^{-2}$. The penetration does not depend on

frequency above f = 5.5 GHz, as seen from Table II.3. The calculations for side launch are given in Table II.4. The deposition is there restrained to the peripheral region. The current drive efficiency can be higher for several cases due to the absorption at lower electron density.

Results from the calculations with the BARANOV code are shown in figures II.1 and II.2. The LH generated current density profiles are similar for both frequencies of 5.5 and 8 GHz, as seen from Fig.II.1. Equatorial launch favours more peripheral deposition at the higher frequency. With top launch the waves penetrate in all cases down to r/a = 0.3, with the deposition profile centered around r/a = 0.5. The maximum of the LH driven current can be shifted between r/a _ 0.5 and r/a ~ 0.7 by varying $N_{||}$ in the range $N_{||}$ = 1.5 - 2.5. The sensitivity of the LH absorption zone to electron temperature variations has been studied in the range T_{eo} = 15 - 25 keV, assuming a parabolic radial profile. The deposition zone is gradually shifted towards the periphery when the temperature increases. Even for the highest temperature the peak is located at r/a ~ 0.75 (Fig.II.2).

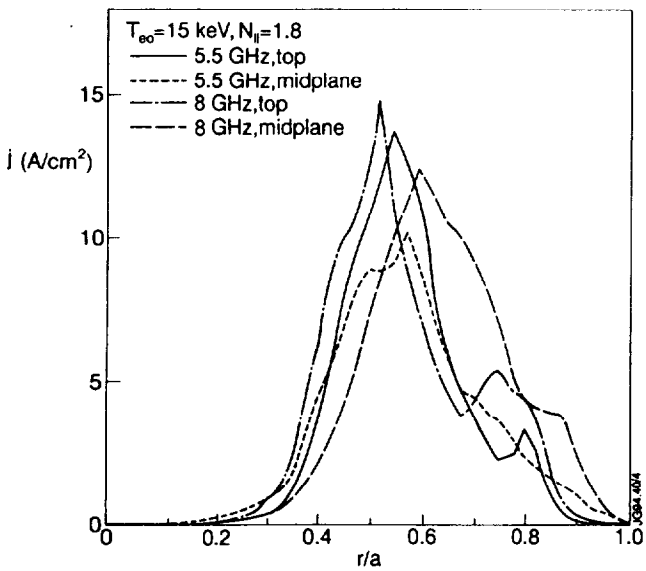

Fig. II.1 : LH current deposition profiles for an ITER steady state case for two different LH frequencies and two different poloidal locations of the LH launcher; P_{LH} = 50MW.

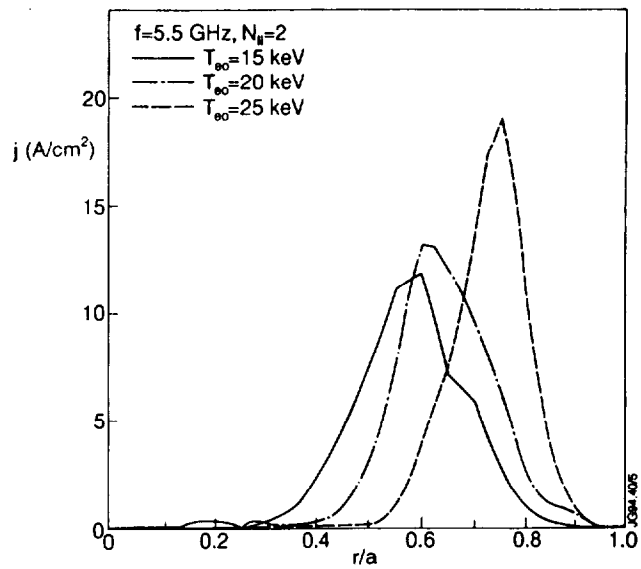

Fig. II.2 : LH current deposition profiles for an ITER steady state case for two different central electron temperatures with LH waves at 5.5GHz with power P_{LH} = 50MW.

Power and current deposition profiles from both codes are compared in Fig.II.3 for f = 5.5 GHz and f = 8 GHz. Results from the BANDIT code are plotted in the top part, results from the BARANOV code, using the 2-D (momentum space) Fokker-Planck equation, in the bottom part of Fig.II.3. The electron density and temperature profiles used for these calculations are included in the top left hand side figure. In all cases LH waves with a spectrum peaked at $N_{||}$ = 2 are launched from the top of the plasma. The shape of the radial profiles is similar in all cases. The deposition profiles peak around r/a ~ 0.5. The LH driven current is

somewhat lower in the BARANOV calculations, mainly due to higher collisional damping at the edge.

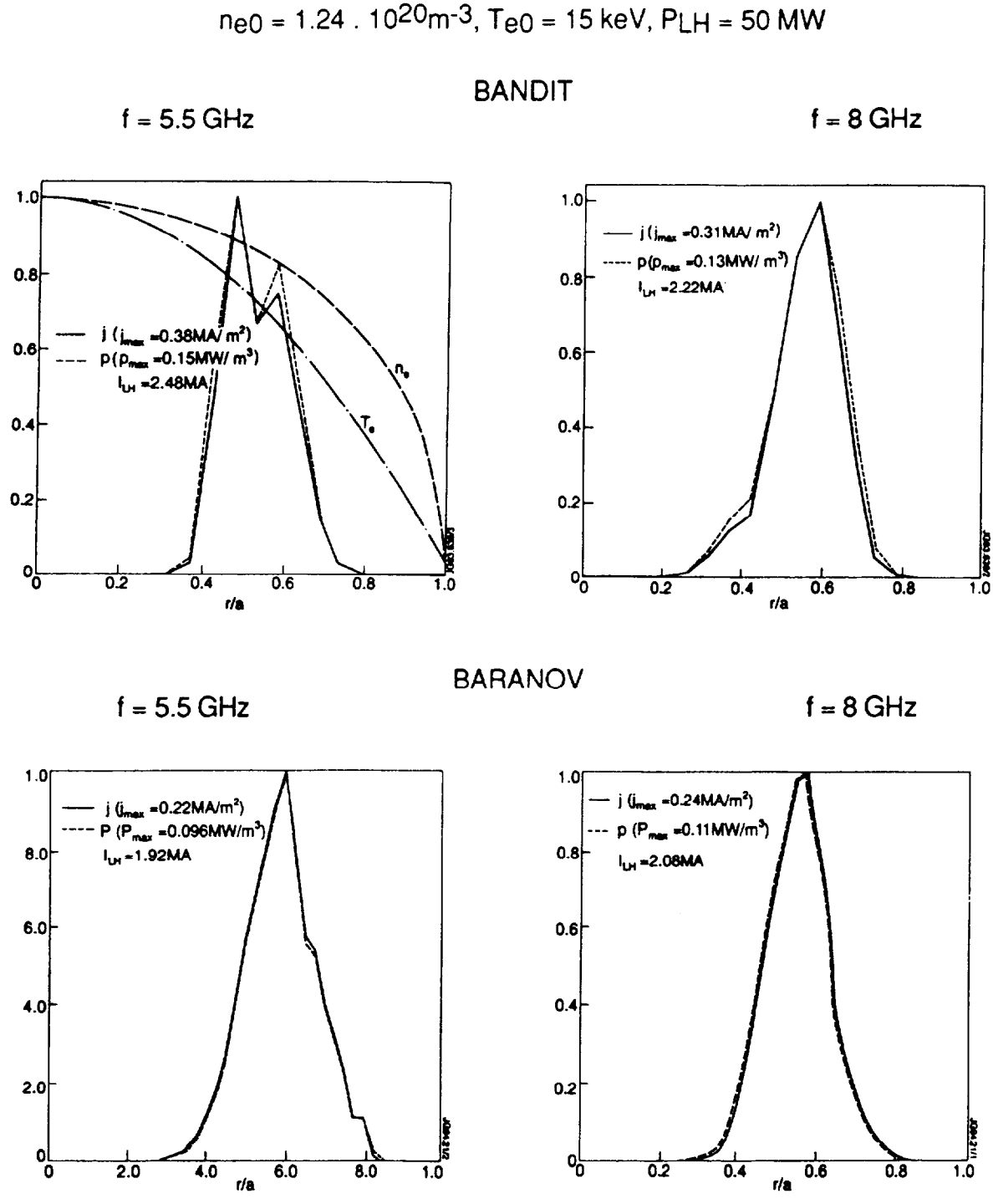

Fig. II.3 : Comparison of the LH current deposition profiles for the ITER steady state case from calculations with the BANDIT and the BARANOV codes for two different LH frequencies and top launch.

(a) f = 5.5 GHz

$N_{//}$	I_{rf} (MA)	r/a (peak)	
-1.3	**1.64**	**0.85**	
-1.5	**2.16**	**0.8**	
-1.8	**1.91**	**0.7**	
-2.0	**2.48**	**0.5**	**Best penetration**
-2.5	**1.78**	**0.75**	
+1.3	**-1.49**	**0.75**	
+1.5	**-1.8**	**0.8**	
+1.8	**-1.65**	**0.8**	
+2.0	**-1.61**	**0.85**	**Good counter CD**
+2.5	**-1.23**	**0.85**	

(b) f = 8 GHz

$N_{//}$	I_{rf} (MA)	r/a	
-1.3	**1.63**	**0.8**	
-1.5	**2.55**	**0.85**	
-1.8	**2.85**	**0.8**	
-2.0	**2.22**	**0.55**	**Best penetration**
+1.3	**-1.4**	**0.7**	
+1.5	**-1.76**	**0.75**	
+1.8	**-1.68**	**0.8**	
+2.0	**-1.61**	**0.85**	

Table II.2 : Variation of the LH-driven current and penetration with $N_{||}$ for top launch ($n_{eo} = 1.2\ 10^{20}\ m^{-3}$)

f (GHz)	I_{rf} (MA)	r/a (peak)	
4.5	**2.11**	**0.65**	
5.5	**2.48**	**0.5**	
7	**2.4**	**0.55**	
8	**2.22**	**0.55**	
10	**2.69**	**0.5**	**(broad profile)**

Table II.3 : Variation of the LH-driven current and penetration with ($N_{//}$= 2) with frequency for top launch (n_{eo} = 1.2 10^{20} m^{-3})

II.2. "JETTO" Transport Code Calculations

Transport code calculations with the 1.5-D code JETTO were run with the LH power and current deposition profiles calculated at each time step with the Pereverzev model [4]. This model has been implemented into the transport code as it provides the short computational times required in time dependent modelling. The steady state conditions of the main scenarios were modelled in addition for cross checks with the ray tracing codes BARANOV and BANDIT3D, using the density and temperature profiles and the equilibrium configurations obtained in JETTO as input. Particle transport is not calculated in these runs with JETTO, but the density profile is prescribed with a radial dependence taken as $(1-(r/a)^2)^{0.5}$. Energy transport is described with a model developed on the basis of L- and H-modes in JET discharges [6]. For the ITER modelling calculations, the radial dependences of electron and ion heat conductivity are taken as for L-mode plasmas, with a constant multiplier. A total power input between 50 and 100 MW absorbed power from LH alone was applied in these calculations. Additional control of the current density in the central region is obtained with FWCD. The power redistribution between LHCD and FWCD was varied in the transport code calculations, with a total power from both rf systems together up to 100 MW.

Current profile control is achieved most efficiently with LHCD in a wide operation regime, as high current drive efficiencies are obtained at low β and with off-axis current drive at high β. During the ohmic ramp-up phase of the plasma current, the LH waves can penetrate to the central region and generate a LH-driven current profile peaked on axis. This slows down the penetration of the ohmically driven current. After start of heating through the fusion power production, the shape of the current profile is almost frozen in and any further evolution would take place on an extremely long time scale.

(a) f = 5.5 GHz

$N_{//}$	I_{rf} (MA)	r/a (peak)
-1.3	**0.85**	**0.8**
-1.5	**3.19**	**0.9**
-1.8	**2.8**	**0.8**
-2.0	**2.34**	**0.8**
+1.3	**-0.8**	**0.75**
+1.5	**-2.25**	**0.8**
+1.8	**-2.76**	**0.7**
+2.0	**-2.79**	**0.7**

(b) f = 8 GHz

$N_{//}$	I_{rf} (MA)	r/a (peak)
-1.3	**0.96**	**0.75**
-1.5	**2.58**	**0.9**
-1.8	**2.54**	**0.75**
-2.0	**2.34**	**0.65**
+1.3	**-0.7**	**0.75**
+1.5	**-2.57**	**0.8**
+1.8	**-2.62**	**0.7**
+2.0	**-2.14**	**0.6**

Table II.4 : Variation of the LH-driven current and penetration with $N_{//}$ for side launch (n_{eo} = 1.24 10^{20} m^{-3})

Two model cases were developed for ITER operation with heating and current profile control by LHCD and FWCD. The main parameters and the results from the JETTO transport code calculations are given in Table II.1. In both cases 50 MW from LHCD and the FW system each are applied.

II.3. Standard High-Current Operation

In the standard ITER case with 25 MA plasma current and a toroidal magnetic field of 6.2 T, control of sawteeth and m=1 and m=2 modes throughout the discharge can be achieved by start of LHCD during the current ramp-up. A plasma current ramp-up rate of 0.5 MA/s is applied.

The FW system is used for central current control in the flat-top phase and additional heating. The temporal evolution of the plasma current, the non-inductive externally driven currents and the bootstrap current are shown in Fig.II.4. The bootstrap current rises after ignition to I_{bs}=9MA. Non-inductive currents of I_{LH} = 3.1 MA and I_{FW} = 0.5 MA are driven externally. A flat shear reversal is produced within the inner half of the plasma by LHCD application during the ramp-up and maintained into the stationary phase when LHCD drives the current off-axis. The q-profile in a late phase during flat-top is shown in Fig.II.5. Stationary conditions are not yet established at this time, 600s after the initiation of the discharge. The central

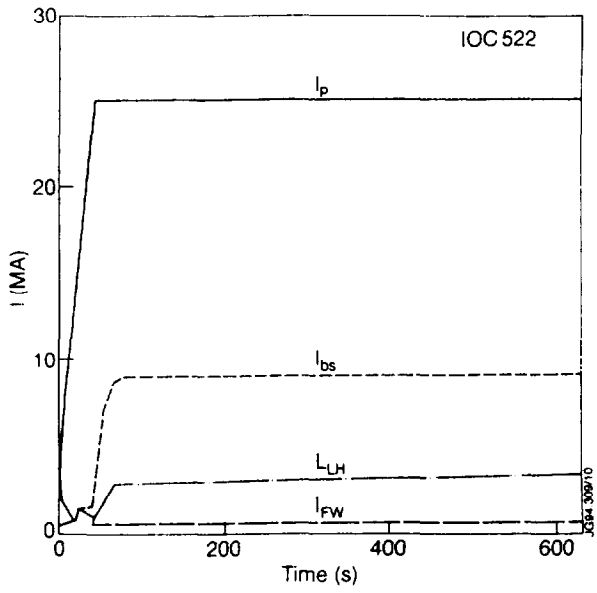

Fig. II.4 : Time evolution of plasma current, bootstrap current, LH-driven current and FW-driven current in JETTO transport code calculations for the ITER standard case with 25MA as given in Table II.1.

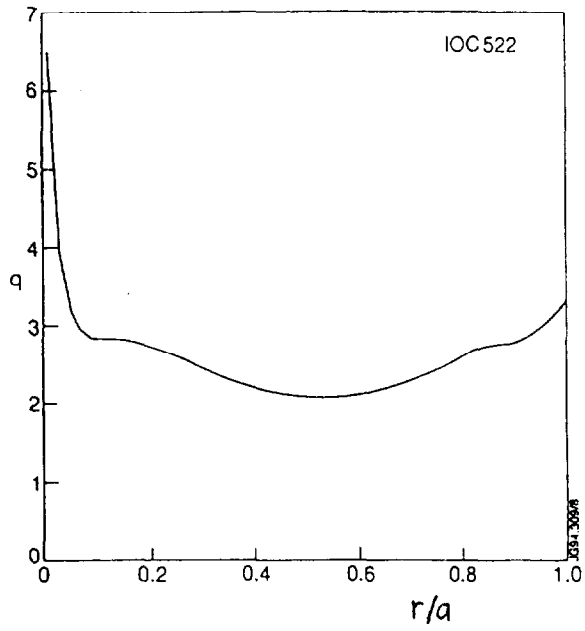

Fig. II.5 : q-profile during the flat-top phase of the ITER standard case with 25MA as given in Table II.1.

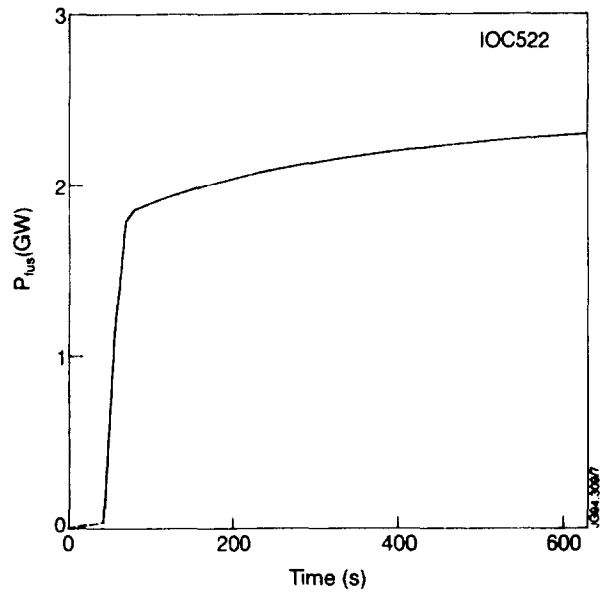

Fig. II.6 : Time evolution of the fusion power output for the ITER standard case with 25MA as given in Table II.1.

q-value is high, close to 7. The control of the central q-value requires careful adjustment of amplitude and waveform of Fast Wave current drive in the early phase of the discharge when the bootstrap current builds up off-axis. The q-value stays above 2 over the whole plasma cross

section. No sawteeth, m=1 and m=2 modes will therefore be excited throughout the whole discharge. The temporal evolution of the fusion power, approaching a steady state value of 2.3GW for this standard case is shown in Fig.II.6.

II.4. Steady-State ITER Operation

II.4.1. Advanced, MHD-stable scenario based on 'JETTO' transport

An advanced scenario for steady state operation of ITER at a lower plasma current of 13.5MA and a magnetic field of 5T has been developed by combining LHCD and FWCD with a high fraction of the bootstrap current. Enhanced confinement may be expected in high bootstrap current discharges, as seen in recent experiments on DIII-D, JET, JT-60, TFTR and TORE SUPRA. For steady state scenarios on ITER, improved confinement is essential in order to maximise the bootstrap current and to minimize the power requirements for non-inductive current drive. Therefore a multiplier giving confinement times about a factor 2.8 above L-mode has been used in the transport code calculations. The results of the JETTO transport code calculations were analysed with the MHD stability code CASTOR for the stability of ballooning, external kink and infernal modes. MHD stability calculations for flat and hollow current profiles show that ballooning modes can grow unstable in conditions with a peaked pressure profile and low central q values. Stable operation, however, is obtained if q is high enough in the central region ($q \geq 3$) and the minimum in q for hollow current profile cases is located in a region of low pressure. High bootstrap current scenarios imply hollow plasma current profiles. Infernal modes can be excited when the minimum in q is located near rational surfaces. Passages from positive to negative shear have to be avoided therefore in regions of high pressure. A stable route to non-monotonic q-profiles has been found with the specific ramp-up scenario which combines LHCD and a fast ohmic ramp-up [3]. The hollow current profile with shear reversal over the whole central region is thereby formed in an early low-ß phase and frozen in by additional heating. Extension to steady-state operation requires then only slow adjustments of the current drive systems, as the time constants for current profile changes are long. Full feedback control of the current profile with external drive by LHCD and FWCD, however, has still to be demonstrated. These studies are part of the Advanced Tokamak scenario program foreseen on JET and their extrapolation to long-pulse steady-state operation will be investigated on TORE SUPRA.

Burn instabilities can be encountered, however, in scenarios with high bootstrap current fractions if the energy transport is linked to the current profile. The transport model used in the JETTO transport calculations takes the following form for the heat conductivities:

$$\chi_e \equiv \left(\chi_i - \chi_i^{neo}\right)/3 \equiv \alpha_1 \frac{(T_e)^{1/2}}{n_e q R} + \alpha_2 \frac{\nabla(n_e T_e)}{n_e B_t} q^2$$

These transport coefficients were derived from the analysis of experimental data in L- and H-mode discharges on JET[11]. The dependence on the local q-value implies a strong internal coupling between the current profile and the fusion power output in burn conditions where the heating power input is delivered by the fusion power output. Fusion power is determined by the plasma energy content which in turn depends on the current profile. The temporal evolution of the fusion power output is shown for several cases with different composition of central and off-axis current drive from FWCD and LHCD in Fig.II.7. Oscillations in the fusion power output are excited if the q-value in the center rises too much with dominant off-axis current drive. The time constant of these oscillations is roughly given by the geometric mean value of confinement time and resistive time for current profile changes. With a combination of LHCD and FWCD with 50MW from each system, central and off-axis current drive are balanced to give constant fusion power output.

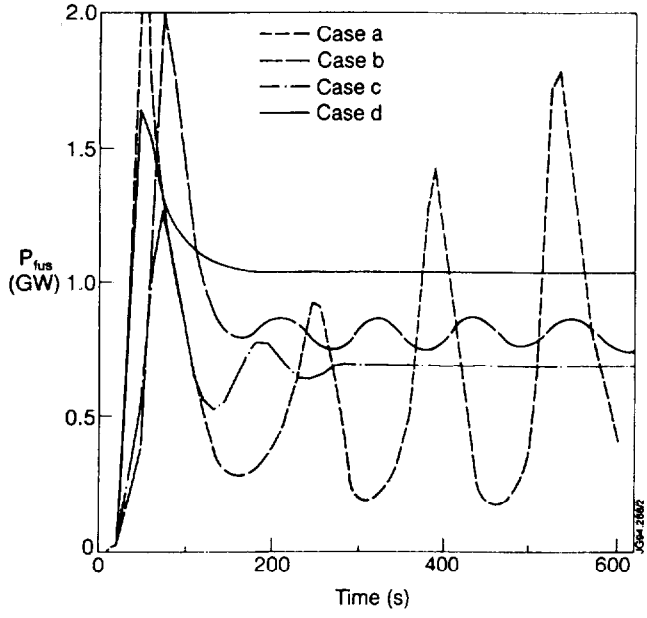

Fig. II.7 : Fusion power ouput for several cases with different compositions of central and off-axis current drive from FWCD and LHCD in steady state ITER scenarios.
Case a: P_{LH} = 100MW (decreasing after ignition within 600s to 50MW), no FW;
Case b: P_{LH} = 60MW (constant), P_{FW} = 10MW;
Case c: P_{LH} = 70MW (constant), P_{FW} = 15MW;
Case d: P_{LH} = 50MW (constant), P_{LH} = 50MW.

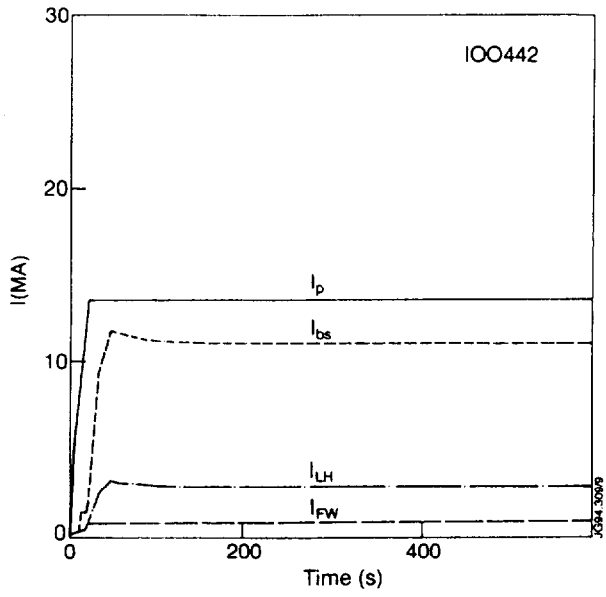

Fig. II.8 : Time evolution of plasma current, bootstrap current, LH-driven current and FW-driven current in JETTO transport code calculations for the ITER steady-state case with 13.5MA as given in Table II.1.

A consistent scenario for steady state operation of ITER is shown in Fig.II.8. The full plasma current of 13.5MA is driven by the combination of 10 MA bootstrap current, 2.8MA LH-driven current and 0.7MA FW-driven current. A wide region of shear reversal is created

inside half of the plasma radius during the ramp-up phase and maintained into flat-top. The q-profile for this case is shown in Fig.II.9. The profile is stable against ballooning and infernal modes. Constant fusion power output is then obtained as shown in Fig.II.7, case d.

I.4.2. ASTRA modelling with Rebut-Lallia-Watkins transport

Other modellings of advanced steady-state scenarios in ITER have been performed independently with the 1.5-D ASTRA code[12] assuming Rebut-Lallia-Watkins (RLW) transport. These studies [13] aimed at investigating the feasibility of advanced steady-state discharges in ITER with a number of constraints considered as required for the proposed scenarios to have a strong potential. These constraints include :

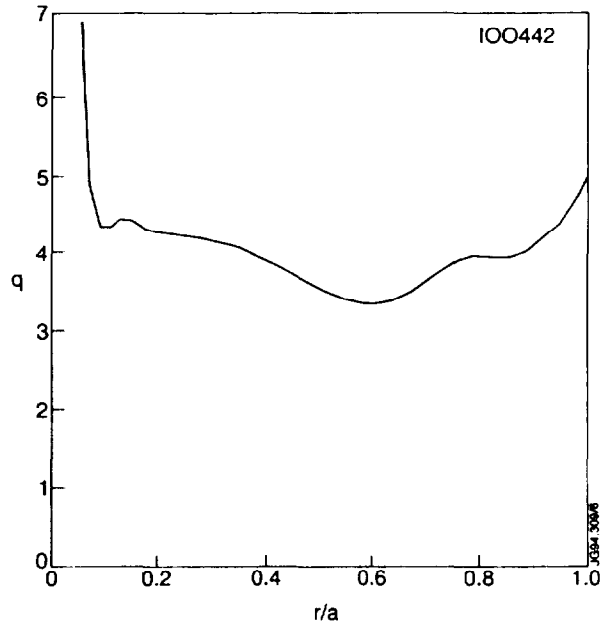

Fig. II.9 : q-profile during the flat-top phase of the ITER steady-state case with 13.5MA as given in Table II.1.

i) production of a significant fusion power, and fusion multiplier Q > 10 ;

ii) operation at a sufficiently high plasma density to meet power exhaust requirements ;

iii) a bootstrap current fraction limited to ~ 70 % of the total current (beyond which the control of the dynamic stability of the discharge appears difficult) ;

iv) current drive efficiencies in agreement with present experiments ;

v) enhancement factor of the confinement with respect to the ITER-89P scaling law not exceeding 2.5 ;

vi) normalized ß ≤ 3.

The obtention of such discharges was found possible in the realm of the RLW transport model when combining the use of Lower Hybrid and Fast Waves. Fig.II.10 illustrates the evolution of various quantities leading to a purely non-inductive stationnary state with P_{fus}=1.3 GW, Q = 14, I_p = 13 MA, q(a) = 5.5, I_{bs}/I_p = 0.66, with a normalized β of 3 and an average density of 0.8 x 10^{20} m^{-3}. Enhanced confinement (by a factor up to 1.5 with respect to the RLW scaling) is beneficial as it maintains stable burn at sufficiently low density for adequate current drive. The effective confinement time is however still 10 to 20 % lower than the ITER-90H ELMy H mode scaling (H_{89P} = 2.4).

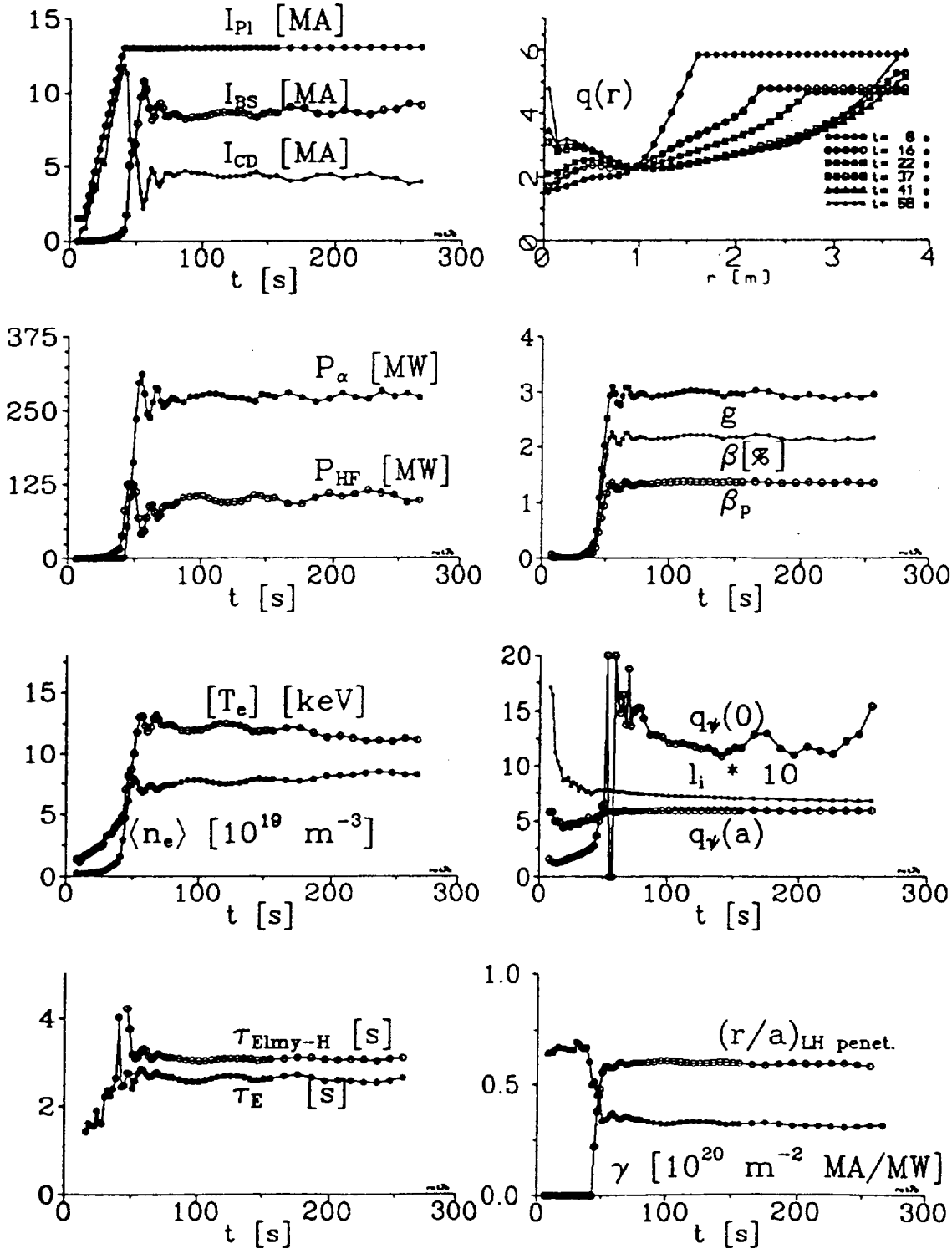

Fig. II.10 : Evolution of various discharge parameters in a scenario leading to purely non-inductive state (ASTRA/RLW simulation).

A transient reversal of the central current density generally occurs at the beginning of the burn phase as a result of the diffusive evolution of the central electric field induced by the off-

axis rise of the bootstrap current, and by other transient changes (temperature, RF power ...). This phenomenon must be adequately feedback controlled (e.g. by slower ramp rates) so that the excursions of the central safety factor always stay within limits which are consistent with the MHD stability of the plasma (see II.4.3).

II.4.3. Feedback schemes for long-pulse current profile control

Studies of the feedback schemes which will be necessary to control the discharge against non-linear interactions between external and bootstrap current generation, current diffusion, heat transport and α-particle heating have been performed with a 1-D time-dependent code (CRONOS). The emphasis and final goal of these studies is to define the proper knobs and feedback loops which will provide optimum control of the q-profile in the various phases of the discharge. Due to the very long burn phases which can be envisaged in these steady-state scenarios, we have considered here rather slow changes in the plasma parameters (current, minor radius, density) in order to avoid large induced electric fields in the plasma bulk at the start of burn. It was found that it is then possible to maintain the pre-formed current profile during the long resistive relaxation of the ohmic components which are unavoidably generated during transients.

i) Low current/low density current profile formation :

Prescribed MHD-stable current profiles with shear reversal in the centre can be obtained through simultaneous PID feedback on the LH and FW powers as well as on the primary flux during the current profile formation phase. An example is shown on Fig.II.11 where the plasma density and minor radius were kept constant during the first 100 seconds and particular values of the safety factor were prescribed at two radii : $q_0 = 3.5$ on axis (controlled by the FW power) and $q(r/a = 0.5) = 2.5$ (controlled by the LH power). In this example, the total plasma current adjusts freely to the required q-profile and the surface loop voltage is controlled ($V_s \propto dP_{LH}/dt$) such as to provide a prescribed fraction of the flux which is necessary to obtain this profile while maintaining a small negative electric field in the plasma core [14]. A small negative electric field is helpful to produce a reversed shear in the centre through the neo-classical resistivity profile. At the end of this phase the plasma current then reaches 5MA while 25MW of LH power (+ 10MW of FWCD) nearly drive the total current so that the plasma is close to an equilibrium fully non-inductive state.

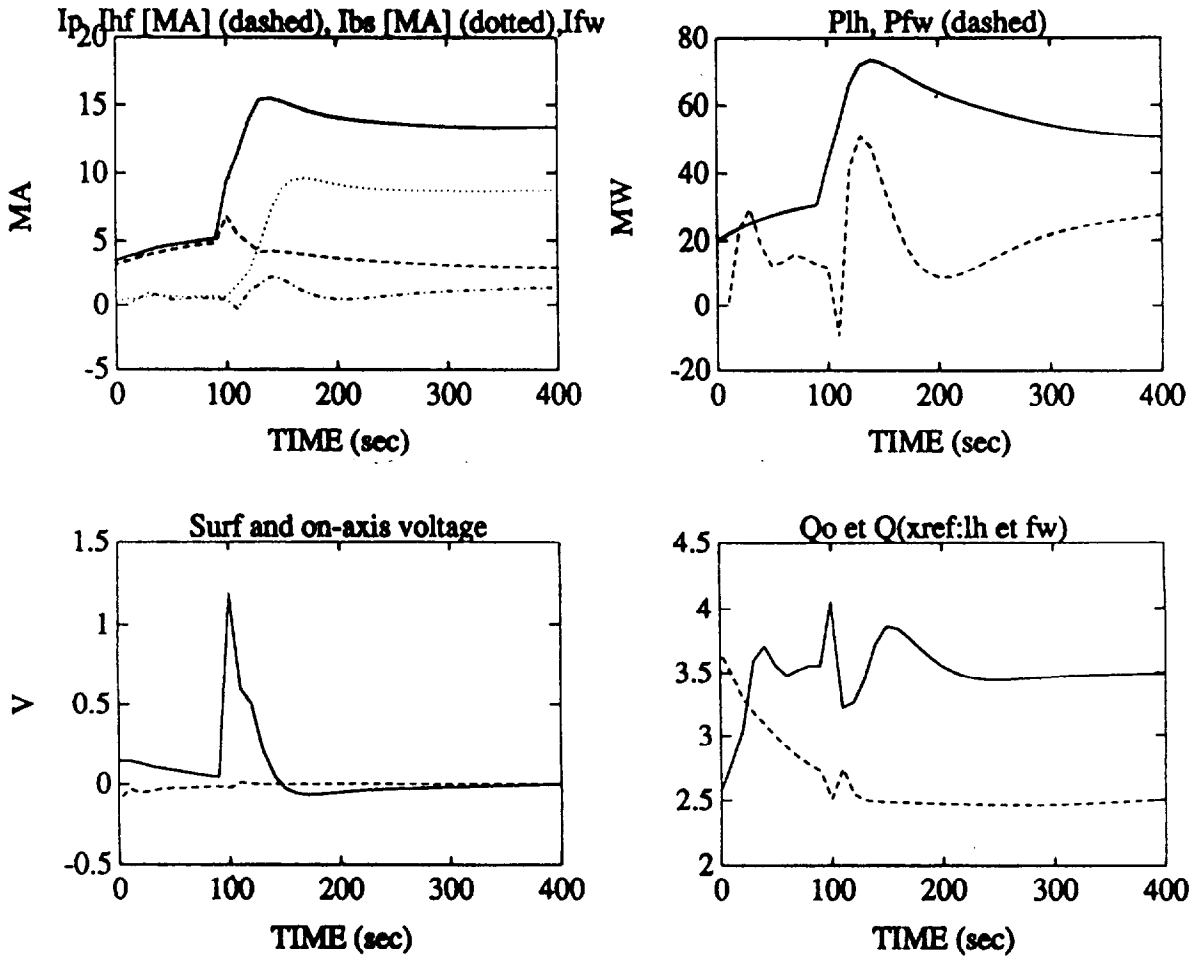

Fig. II.11 : Time evolution of the various current components, LH and FW powers, surface voltage, q_0 and $q(r/a = 0.5)$ during a scenario with feedback control of the q profile.

ii) Plasma aperture expansion, fueling and α-power rise :

During a second phase (100-130s) the plasma current is raised through an aperture expansion to bring the discharge to its full cross-section. The current then rises up to 13.5MA because of the increase of the LH, FW powers and surface loop voltage which are bound to maintain the same q-profile. At the same time the density is increased up to a level which is determined by the required fusion power yield. The effect of α-particle heating and external power rise is to increase significantly the bootstrap current contribution up to 9MA. Transients are then observed on the electric field profile, inducing a slight oscillation in the safety factor on axis (q_0) for about 100 seconds. The q-profile evolution is shown on Fig.II.12 for the first 400 seconds of the pulse. The fusion power and q-profile must be simultaneously controlled throughout the burn phase while the electric field slowly decays.

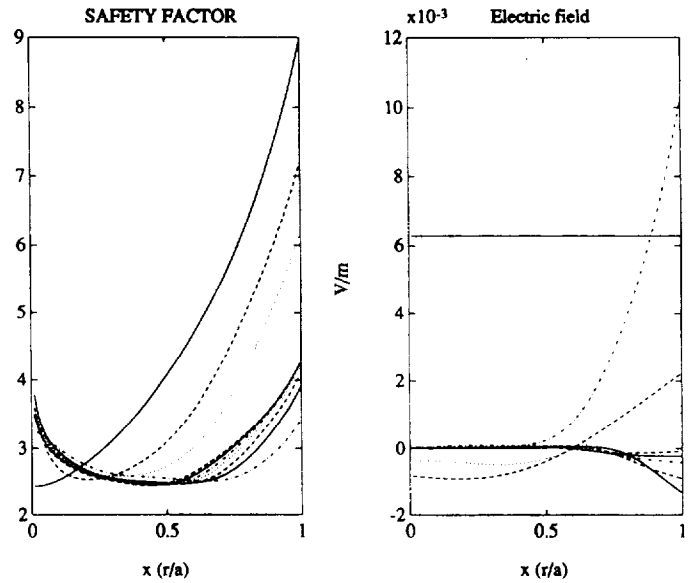

Fig. II.12 : q-profile and electic field at various times during the simulation shown in Fig.II.11.

iii) Long-term evolution and non-linear couplings :

Once the required ignited plasma has been obtained (t=250s.), a slight electric field (yet driving a significant central ohmic component, j_{OH}) still persists in the plasma. When it is negative, a feedback loop which simply links the external FW power to the measured q values at r=0 becomes unstable because of the coupling between the external power and the change in the central plasma conductivity (σ_0). For example, in order to prevent an increase of q_0 on a resistive time scale, the FW power must slowly increase and therefore the central temperature increases. The evolution of the system is then governed by $dP_{FW}/dt \rightarrow d\sigma_0/dt \rightarrow dj_{OH}/dt \sim -dj_{FW}/dt$, so that q_0 is nearly constant and never reaches the prescribed value while the FW power continuously increases.

Instead, a given (but unknown) amount of power should be applied such that the central electric field vanishes, and this power should then remain constant throughout the electric field diffusion time.

In order to stabilise the evolution of q_0 and of the FW power on the long term, a scheme based on separate measurements of the ohmic current density and of the non-inductive current density could be more appropriate. Such measurements have been recently made on DIII-D, and are based on magnetic field reconstructions at various times [15]. In ITER this could be done in real time since, thanks to the extremely slow evolution of the current density profile (~ 1000s), one would be satisfied with rather large time slices (e.g. 30s. or more) between two measurements. Such a scheme has been simulated with CRONOS and the previous instability

did not show up. However, non-linear couplings between the fusion power yield, the bootstrap current density and the external power required to maintain the q-profile can still make the long-term burn control delicate and should be further studied. For instance, they can result in a limit cycle such as shown on Fig.II.13 where the plasma current, temperature and fusion power oscillate with a period of about 2000 seconds. On such a long time scale, it is anticipated that the oscillations could be removed by an additional control of the plasma density, but this has not been tested here.

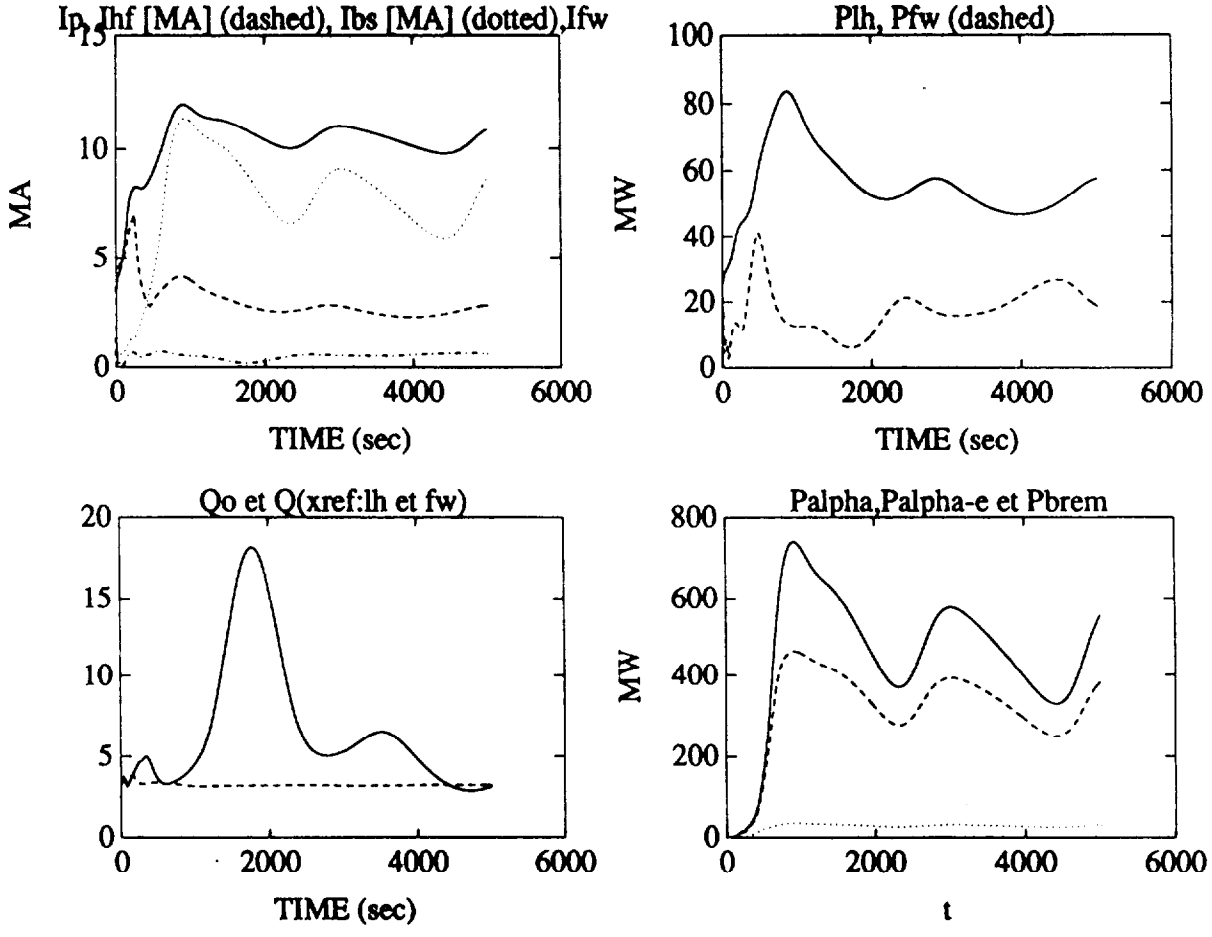

Fig. II.13 : Example of non-linear oscillations during the long-term evolution of the discharge with feedback control of q_0 based on a real-time measurement of the central ohmic component.

Feedback stabilization studies are presently being pursued in the aim of identifying the most practical current drive methods and feedback schemes in order to come up with a reliable steady-state operation scenario.

III. OUTLINE DESIGN OF A LOWER HYBRID LAUNCHER FOR ITER

III.1. Introduction

This section describes the proposed launcher, the ITER parameters used in the design, and the limiting temperatures and stresses arising in the launcher. The level of detail is similar to that of the TAC-4 report. Insufficient information is available to consider in detail the integration of the launcher onto ITER, but outline proposals are presented on the basis of the available data.

III.2. The Design Basis

The outline design to be presented here is based on the ITER data given in the TAC-4 report. Parameters below marked with an * are not yet defined by the ITER Central Team but are understood to be a realistic design basis. The following key data are noted :

III.2.1. ITER Environment

Burn lifetime	10,000 hours *
Toroidal magnetic field at grill mouth	4T
Vertical field at grill	1T
Neutron power at grill	
Mean	1 MW/m^2
Spatial peaking	1.5MW/m^2
Temporal and spatial peaking	2.4MW/m^2
Neutron fluence at grill (mean)	10E26/m^2
Plasma radiation power density at grill	0.5 MW/m^2 *
First wall temperature	200C

III.2.2. Cooling system

Coolant	Water
Inlet Pressure	20 bar
Outlet pressure	15 bar
Inlet temperature	150C
Max outlet temperature	200C

III.2.3. Vacuum vessel

Design internal pressure	20 bar
Design temperature	300C
Applicable code	ASME VIII
Material	Stainless steel

III.2.4. Disruptions

Plasma current decay	10 MA/msec
Heat blast	2 MJ/m^2 *
Conducting shell current decay	0.05 MA/msec *
No of disruptions	1000 *
Halo current	0.4 MA/m toroidally

III.2.5. Main Horizontal Port Dimensions

The available area for use by the launcher is taken to be 1650 mm high by 1060 mm wide. This is after allowance of a height of 300 mm at the bottom of the port for services to the lower blanket module.

III.3. RF Specifications

The physics requirements and operating scenarios of the Lower Hybrid system were discussed in section II of this report. The following key parameters form the basis of the design ;

Frequency:	5 GHz
Pulse length	CW
$N_{//}$	2

The system is modular, with each module occupying one main horizontal port. The generator power to each module is 24 MW.

III.4. Conceptual Design of the Launcher

The physics of LH current drive defines the frequency (5 GHz) and the optimum spectrum, in this case with a central $N_{//}$ of 2. These define the wavelength across the grill as about 30mm. The total width of the port thus represents about 40 wavelengths. In this case, the spectrum is very narrow and the directivity high. A phase shift of 135 degrees between guides, with an average pitch between guides of 11.25mm, have been chosen to minimise the number of waveguides whilst maintaining a near optimum spectrum. The wall thickness is a compromise between maximising the coupled RF power and improving the robustness of the grill in the ITER first wall environment. A value of 3mm has been adopted, which leaves an average of 8mm width for each waveguide.

To reduce the total number of waveguides they are oversized in the poloidal direction up to the plasma antenna interface.

Cooling of the waveguides at the grill mouth, which are subject to the intense neutron flux and plasma radiation at the first wall, requires the provision of active cooling channels close to the mouth. A convenient means of providing space for such channels is the use of passive waveguides for every second guide at the grill , as illustrated in fig.III.1 [16] and III.2. The depth of the passive waveguides is chosen to optimise the spectrum and turns out to be about 16mm for the envisaged grill. This enables cooling of the grill mouth by conduction to cooling channels behind the passive waveguides, as in fig.III.2, provided high conductivity materials are used, for example copper alloys or possibly beryllium.

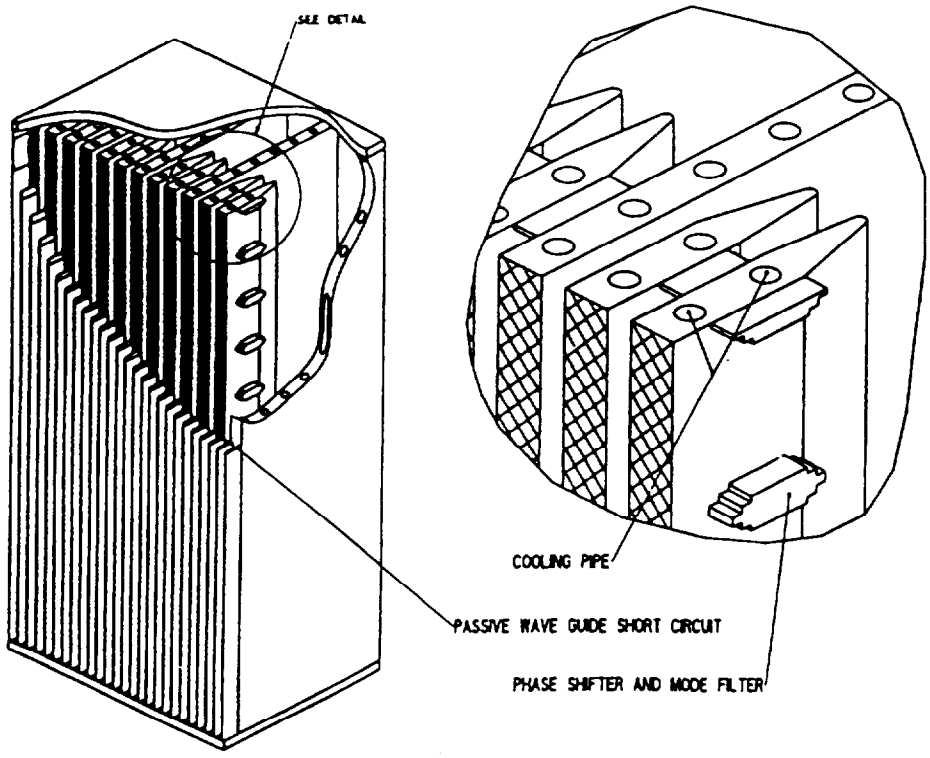

Fig. III.1 : A section through a passive waveguide grill (schematic).

A consequence of this active/passive waveguide structure is that the overall coupled power for a given area of grill could be reduced by a factor two if ones takes into account only a power density limitation in the active waveguides. The acceptable power density is a function of frequency and reflection coefficient. The coupling of the grill to the plasma in ITER is discussed in

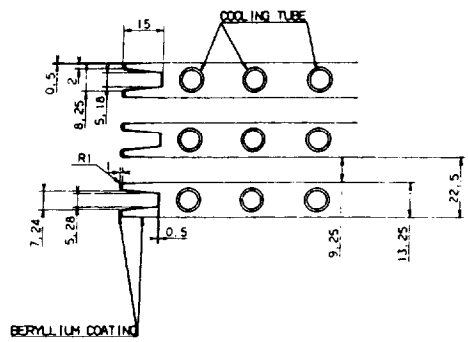

Fig. III.2 : A section through the grill mouth.

Appendix 2. For the conditions anticipated, a power density of 3.8 kW/cm^2 is safe [17] ; given low reflection at the grill and good conditioning, a peak value of 6 kw/cm^2 may be achieved [18]. Multipactor calculations give as a first level of power limitation an electric field of 300 kV/m corresponding to a power density of 4.8 kW/cm^2. For the available port area, the coupled power is therefore in the range 15-24MW per port for the passive active waveguide launcher.

A benefit of the passive waveguide structure is that the grill is typically 60%

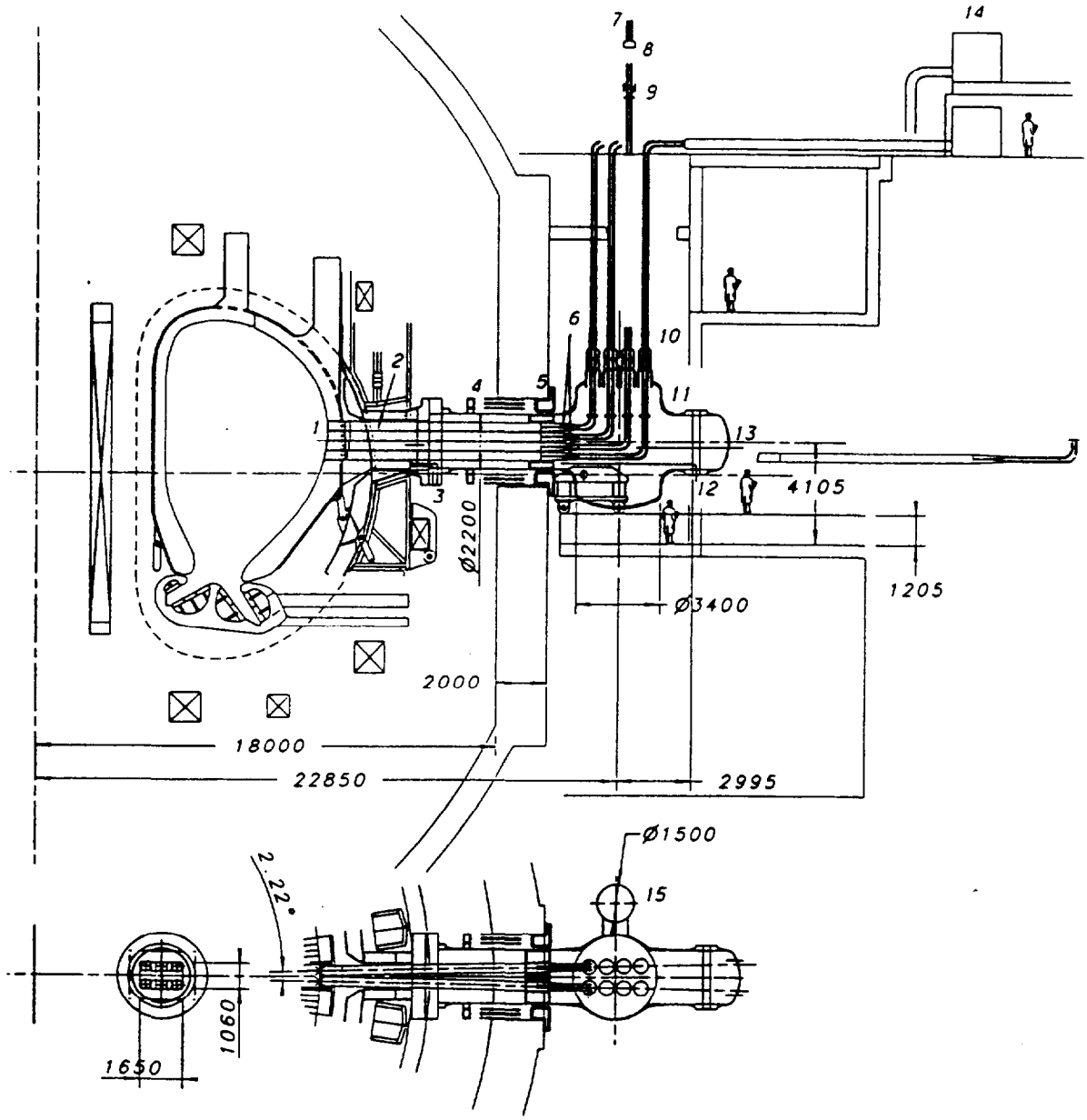

1	Cadre	9	Cooling
2	Hyperguide	10	Waveguide Cooling
3	Lower Shield Services	11	Launcher Vessel
4	Bellows	12	Cadre Cooling
5	Neutron Shielding	13	Hyperguide Cooling
6	Convertors	14	Generators
7	Window Cooling	15	Cryo Pump
8	Windows Sleeve		

Fig. III.3 : A schematic of the launcher on ITER.

dense in this region, and can therefore provide substantial neutron shielding. The length of this 'plug' may be increased to improve the shielding, each meter giving typically two orders of magnitude reduction. The grill may then be viewed as an integral part of the shield. This in

particular enables the full area of the port to be used for waveguides without exposing the TF coils to excessive radiation.

This length of the plug now conveniently accommodates phase shifters and multijunction splitting networks to give the required phase distribution at the grill mouth combined with low reflection from the plug. The plug in turn is excited by 'hyperguides' - large highly overmoded waveguides which offer simple construction, low losses, and excellent vacuum pumping. The section of 373x345 mm operating in TE0,6 mode offers a compromise between mode stability and simplicity of design, whilst a total of eight such modules conveniently fills the available area.

Each module corresponds to up to 3MW of coupled power, reasonably provided by 6 klystrons each of 0.5MW, with one vacuum window per klystron, all based on present technology. Mode convertors are used to couple the six incoming waveguides to the hyperguide.

The launcher is enclosed within a vacuum vessel rated at 20 bar internal pressure as for the torus vessel. The launcher vessel extends through the cryostat inside a double bellows to withstand the cryostat internal 6 bar design pressure. The RF windows are outside the cryostat where the neutron flux can be comfortably below the allowable flux for degradation of the ceramic.

Remote maintenance of the grill is limited to exchange of the hyperguide/plug modules, or their support structure, from outside of the cryostat. These may be re-furbished off-line if required.

The resulting launcher is shown schematically in fig.III.3 and fig.III.4.

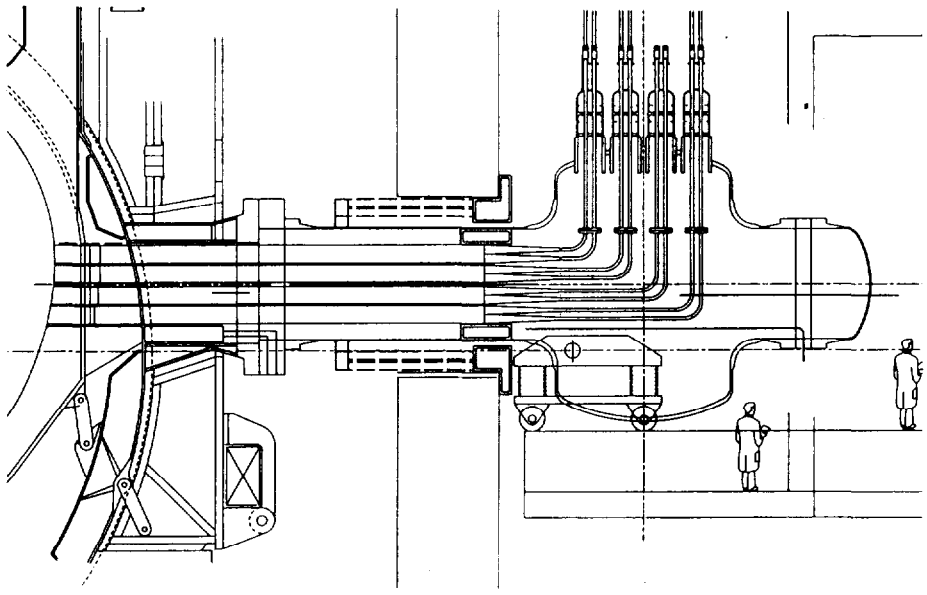

Fig. III4 : A schematic view of the launcher.

III.5. Detail Design of the Launcher

III.5.1. Grill Mouth

It is proposed to use a passive waveguide array in which passive waveguides are set into the thick walls separating the active waveguides. A section of the proposed grill mouth is shown in fig.III.2. The waveguide apertures are approximated flush with the first wall. The phase shift between adjacent waveguides is 135 degrees to give a central $N_{//}$ of 2; the directivity is typically 65 %, taking into account the effect of high order modes at the grill. The depth of the passive waveguide has been optimised to 15mm. The average pitch between waveguides of 11.25mm is required to give the correct $N_{//}$, whilst the wall thickness of 3mm has been chosen to enhance the robustness of the grill against erosion by the disruption heat blast. The tapered wall allows for some re-deposition of first wall material and improves the cooling of the grill mouth. The active waveguide is chosen to be 9.25mm wide compared to 7.25mm for the passive guide. This increases the coupled power for a given power density in the active guides, whilst maintaining a good spectrum.

Appendix 2 discusses the coupling of the launcher at large distance from the plasma, as foreseen in this design.

Details of the RF design of this array are given in Appendix 3.

The grill is subject to intense neutron heating, plasma radiation and RF heating. Neutron irradiation at 1.5MW/m^2 produces a volume heating of typically 15w/cm^3 at first wall flux , depending on the material as shown in table III.1. Plasma radiation gives a peak surface input of 50w/cm^2 over the front face of the grill, the power density distribution over the surface of the waveguides being as shown schematically in fig.III.5. This is the dominant component in determining the temperature and thermal stress in the grill. The RF losses are relatively small, being typically 0.5watts/cm^2 on the side faces of the waveguides in smooth, high conductivity copper alloy, increasing to perhaps 1.5w/cm^2 in re-deposited beryllium of 40% porosity.

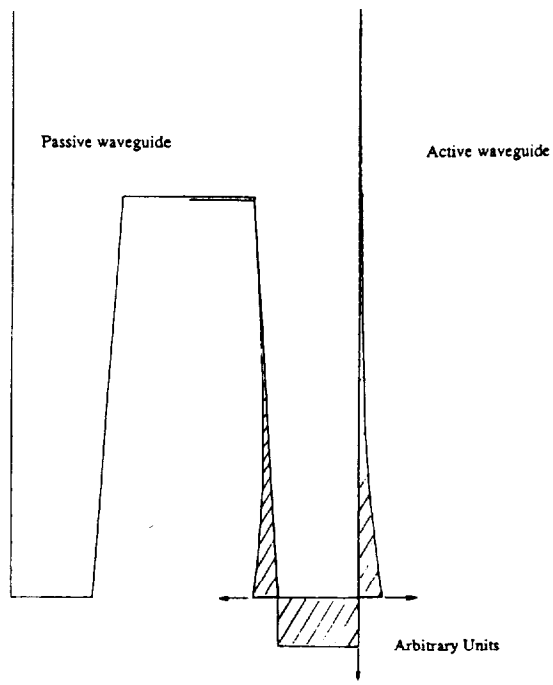

Fig. III.5 : The distribution of incident radiated power over the grill.

Material	Volume heating (w/cm^3)
Inconel	20
Beryllium	9
Copper	20*
Water	15

Table III.1. Heating of various materials due to $1.5MW/m^2$ neutron irradiation at the first wall

The peak temperature and thermal stress in the grill occur on the leading edge of the waveguides. In normal operation, the calculated temperature at the tip of the grill and maximum thermal stress for typical high strength copper alloys (copper/zirconium and copper/alumina) and for beryllium are summarised in table III.2. The former show a comfortable margin of safety, whilst the latter is stressed above the acceptable level. It is therefore proposed to fabricate the mouth from copper alloy with a coating of 1 mm of beryllium similar in thickness distribution to fig.III.7. This would be achieved, for example, by spraying beryllium over a range of angles from in front of the grill. During manufacture, this layer may be "HIP-ped" to improve the mechanical properties of the beryllium.

Material	Temperature (C)	Thermal stress (MPa)	0.2% proof stress (MPa)	Coating stress (MPa)
Copper/zirconium	237	86	220	175
Copper/alumina	238	113	200	182
Beryllium	293	443	230	443

Table III.2. Calculated peak temperature and thermal stress in the grill for various materials.

The coating stress is the stress in a thin beryllium coating on the front face.

($0.5\ MW/m^2$ radiated; $1.5MW/m^2$ neutrons)

During disruptions, the heat blast from the plasma decay will ablate typically 50 microns of beryllium [19] from the first wall and the grill. This will re-deposit in an unknown distribution over the first wall and grill. With a total of 1000 disruptions, it is clear that major erosion from or accumulation on the grill may occur. Erosion with no deposition would seriously erode the 3mm wall at the grill after typically 30 disruptions. Deposition of twice the volume eroded would also lead to failure in a similar number of disruptions by reducing the area of the waveguides. If we assume some intermediate result, it must be anticipated to replace

the grill typically every 100 disruptions, equivalent to typically 1000 hours of operation. This is done by removal of a complete module with access from the cryostat, as discussed below.

It is noted that alternative refractory first wall materials such as boron carbide give much reduced if not zero ablation. The acceptability of such materials as coatings on the grill depends on the associated increase in RF losses. In general, an order of magnitude increase in local RF losses is satisfactory. Thus, such coatings are acceptable provided the surface conductivity is not more than two orders of magnitude higher than copper, or the thickness is small compared to the skin depth. In the case of boron carbide, the skin depth is typically 1mm and coatings of order 100 microns thickness are thus acceptable.

The front 0.8m of the launcher is 60% of solid density , as illustrated in fig.III.6. This both accommodates the splitting and phase control network and serves as a neutron shield. This part of the launcher will be referred to as the 'plug'. The neutron absorbed power density at the first wall for various materials has been shown in table III.1; the corresponding e-folding length in fully dense material is typically 0.1m. The material of the plug must be pre-dominantly copper alloy/water over the front couple of e-folding lengths (400mm) in order to reasonably cool the structure by conduction to internal water channels. These channels are formed by embedding of stainless steel tubes in copper, for example, by vacuum brazing or electrode position, and thus comply with the ITER requirement to use stainless steel for structural containment. This is shown in fig.III.7. It is noted that the brazing into the copper is for heat transfer only; this is not a vacuum barrier. It is anticipated to use many parallel tubes with minimum welded joints inside the torus.

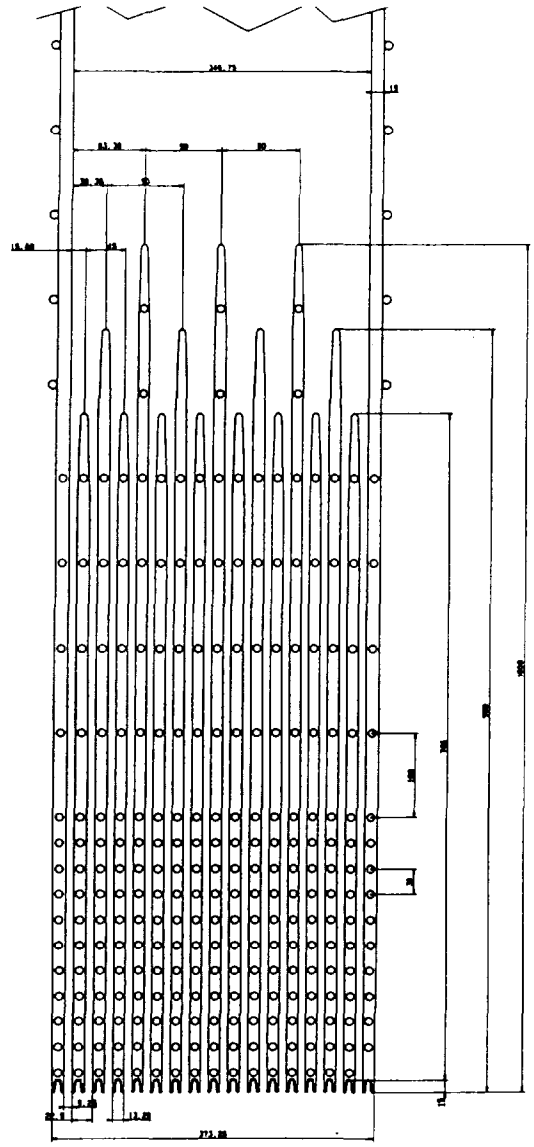

Fig. III.6 : An horizontal section through the plug.

A similar construction is proposed over the rear part of the plug. The density of cooling channels can be much reduced as the neutron flux attenuates with distance into the plug.

Alternatively, stainless steel may be used for the bulk material. In the latter case, the enhanced RF losses are particularly effective at reducing the reflected power due to the multijunction effect. Thus, the single pass transmission factor increases to the fourth power on reflected power from the plug. Whilst this enhances the RF losses substantially (from 1.5% to typically 8% of forward power), it also facilitates the hyperguide mode control.

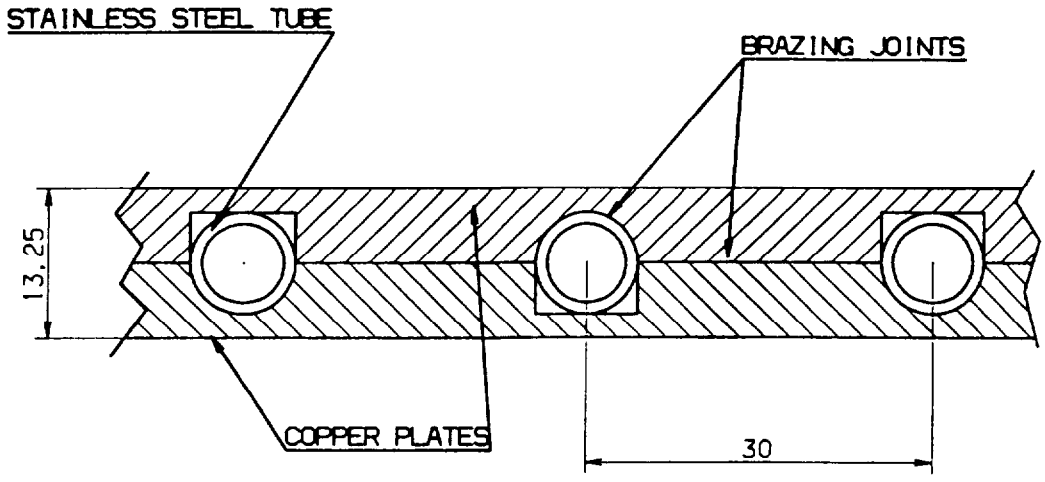

Fig. III.7 : A detail of the cooling tube assembly into the waveguide structure.

The plug is thus typically 60% copper or stainless steel and water, with about 1.5 times the depth of the first wall shield. The neutron shielding will be similar to the shield apart from streaming effects in vertical slices; the solid angle presented by a 9x317 mm slot 800 mm long is typically 10^{-3} and streaming is modest. The neutron transmission through the plug has been modelled numerically. The results are summarised in table III.3. The model does not take account of any attenuation in the structure behind the plug. These results show the effect of the plug as a neutron shield, with typically two orders of magnitude reduction in fast neutron flux at the rear surface of the plug and three orders of magnitude at the cryostat. There is a small region behind the shield strong back to the side of the plug which may need additional screening ; this requires further analysis with a neutronics code. It is then not necessary to include additional neutron shielding in the port to protect the toroidal field coils.

Position	Neutron Fluence ($x10^{26}/m^2$)			
	0-3.5 MeV	3.5-7 MeV	7-12 MeV	12-14 MeV
At grill mouth	0	0	0	1
At rear of plug	0.04	0.001	0.0006	0.008
At cryostat wall	0.0008	0.00004	0.00001	0.001

Table III.3. Computed neutron fluence at various positions in the launcher.

The first wall mean neutron fluence corresponds to typically 10dpa in first wall materials, increasing to 30dpa at the peak fluence. This will produce some degradation of mechanical properties of the material which need to be taken into account in the design stresses. In addition, significant swelling of the material will occur. Actual swelling is difficult to predict as it depends on many parameters, including the metallurgical state, temperature, neutron flux, and stress during irradiation. At the 10dpa mean first wall level, swelling of up to 1% may be expected. This represents 17mm over the height of the grill and 4mm over each of the 8 modules forming the grill. This swelling decreases to negligible levels over the front 400mm. The proposed mechanical design of the plug will accomodate such swelling without jamming in situ or loss of directivity as discussed below.

The materials data required for detailed design of the plug is largely common to first wall materials; any additional requirements or new materials need to be identified and materials test progammes extended accordingly.

III.5.3. The Splitting Network

The plug incorporates the RF splitting network as shown in fig.III.8. The multijunction principle is used whereby sequential E-plane dividers are used to split each incoming waveguide horizontally into eight guides. Phase shifters are incorporated into each of these eight guides to give the required 270 degree phase shift between active waveguides at the grill These shifters are also such that the reflected wave is cancelled at each E-plane junction, with the effect that the reflection co-efficient is squared at each of these 90 degree bi-junctions. With two junctions in series, the reflection coefficient at the hyperguide is reduced to r^4 where r is the reflection coefficient at the grill mouth. This is highly favourable to the stable operation of the hyperguide, but at some expense in enhancing the electric field at the grill (by a factor $1+2r+2r^2+2r^3+r^4$) if the reflection coefficient at the grill is high. These design principles have been verified on existing launchers at Tore Supra, JET and JT-60.

The generous length of the plug enables the use of long phase shifters which reduces the peak electric fields in the active waveguides and will play also the role of mode filters. This field appears to determine the limiting power density in the launcher. Extrapolation from previous data leads to a safe design figure of 3.8kW/cm^2 at 5 GHz, taking account of the effect of multiple reflections within the multijunction. This corresponds to 15 MW/m2 over the area of the grill mouth. With optimum conditioning and low reflection at the grill, up to 6kW/cm^2 may be obtained, equivalent to 24MW/m^2. Single surface and two surface multipactor resonances have been analysed for a waveguide width of 9.25mm. The lowest resonance occurs for two surface multipactoring at an electric field of 300kV/m, which corresponds to 4.8kW/cm^2 in the active waveguides and 20MW/m^2 at the grill.

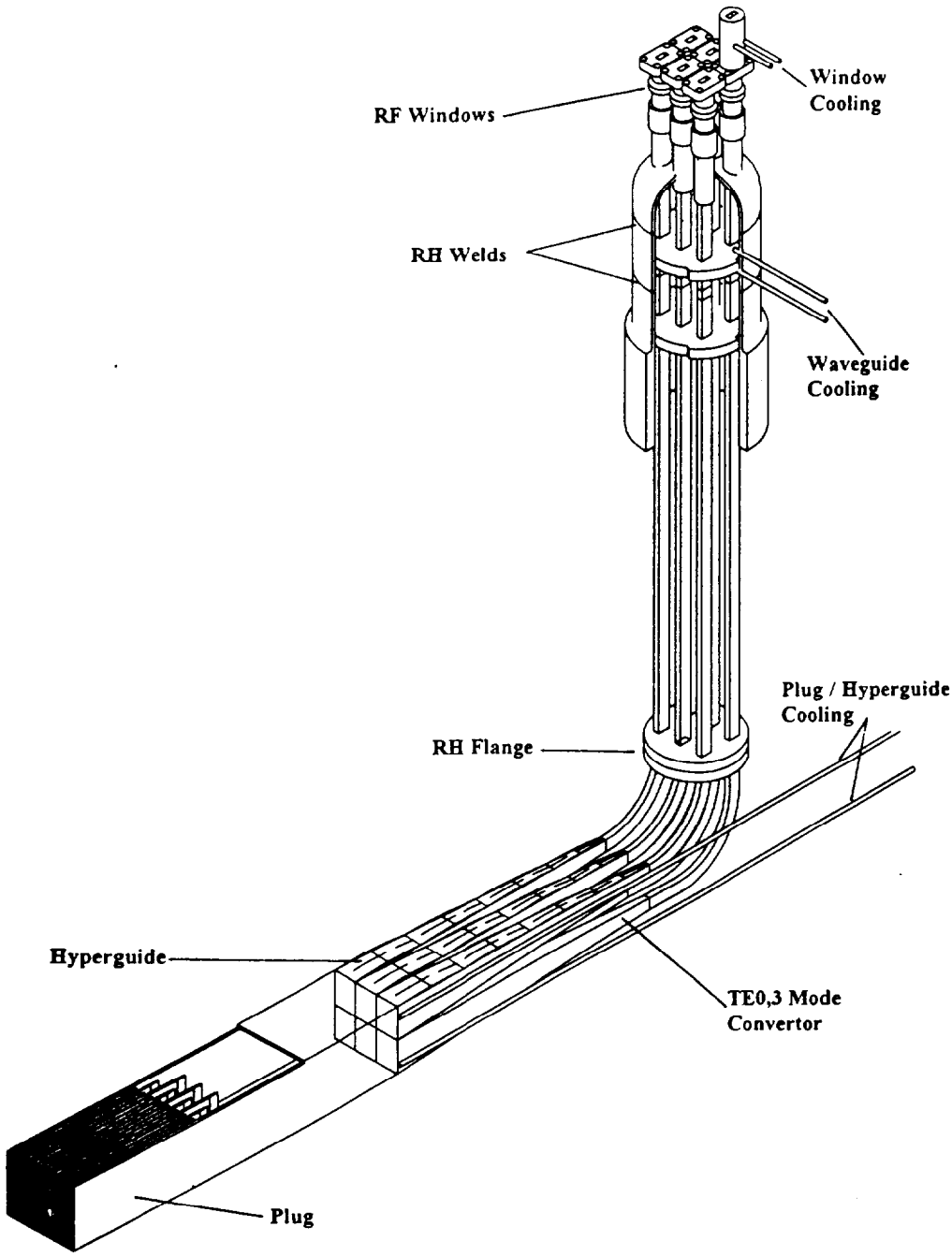

Fig. III.8 : A schematic view of one RF module from the window to the grill.

Phase shifters are used in all waveguides to provide mechanical support to the vertical sections. The phase tolerance required at the grill is typically 10 degrees. This corresponds to a tolerance on waveguide height over the length of the plug of typically 1mm in the 317mm overall height of the module during initial manufacture. Subsequent swelling during irradiation is important only to the extent that differential swelling occurs between adjacent waveguides. over the frontal area of the module. Over the length affected, a tolerance of 1% on waveguide

height is acceptable - as this is typical of the total swelling, differential swelling will not degrade the spectrum significantly.

In the phase shifters, each waveguide operates in the TE0,1 mode. Apart from the phase shifters, there are no horizontal walls dividing the grill and each waveguide operates in the TE0,6 mode. There are 16 such guides per module, to give a total of 128 active and 136 passive waveguides at the grill mouth.

III.5.4. The Hyperguide

It is proposed to use 'hyperguides' to couple power to the plug. A hyperguide is a rectangular waveguide operating in a high order TE0,n mode. The mode number n is chosen to match the number of waveguides in a vertical column of the grill mouth. The hyperguide is excited in the desired mode by appropriate design of the coupler. Extensive modelling and testing of a low power model operating in TE0,12 mode has shown such a guide to be feasible. Details of the hyperguide design and calculation are given in Appendix 4.

The use of hyperguides much simplifies the mechanical design of the launcher, and also offers much reduced losses and outgassing, each being about proportional to the surface area, and much improved vacuum pumping. The hyperguide spans the sensitive area of electron multipactor resonance and may be expected to much facilitate conditioning of the launcher, with beneficial effect on the power density and coupled power to be achieved in the launcher.

The difficulty in using hyperguides arises from the need to suppress unwanted modes. Experience with low power tests and modelling suggests the use of TE0,6 guide to be safe. It is therefore proposed to use such a guide with a section of 346x373 mm. The associated plug has the same area and such 8 sections with the associated support structure conveniently fill the area of the port as shown in fig.III.11. The total frontal area of waveguides is then $1m^2$ and the coupled power is typically 20MW.

The proposed hyperguide material is copper alloy, with discrete stainless steel water cooling tubes brazed to the sidewalls for cooling and baking of the waveguide. The use of high conductivity coatings on

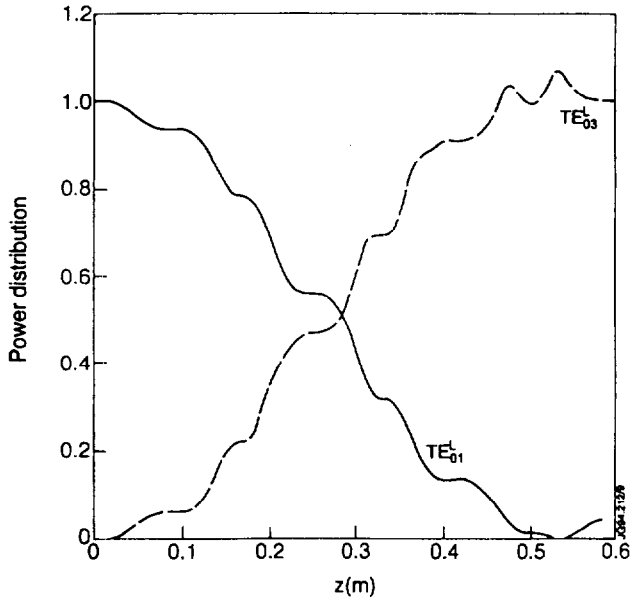

Fig. III.9 : Calculated power distribution in the TE0,1/TE0,3 mode convertor.

otherwise lossy materials such as stainless steel complicates the cooling and raises serious and unnecessary risk with the long-term adherence of the coating. Uncoated vanadium alloy would be an acceptable compromise. Similarly, no anti-multipactor coating is envisaged. Such coatings increase the RF losses and the outgassing, and also raise serious adhesion problems in the ITER environment.

The proposed design uses six TE0,3 mode convertors connected in a 3x2 array to the hyperguide, as illustrated in fig.III.8, to excite the TE0,6 mode in the hyperguide. The proposed TE0,3 mode convertors are made of a rectangular waveguide with a sinusoidal shape of the larger dimension having a geometric period which is the beating wavelength between the mode at the input and that at the output. The amplitude of the modulation and the number of waves are fixed by the desired conversion efficiency. The theory of such a mode convertor has been used to design a similar unit for use on the next Tore Supra 3.7GHz launcher [20] This convertor has a measured 99% conversion efficiency in agreement with the theory [21]. The same theory has been used to calculate the power distribution in the proposed ITER convertor taking account of both forward and reflected waves, as shown fig.III.9. Details and calculations on the mode converter are given in Appendix 5.

III.5.5. The Klystrons, Vacuum Windows and Connecting Waveguides

Each hyperguide has the potential to couple 3 MW. This can be supplied by six 0.5MW klystrons using existing technology. The klystrons would be located in a generator hall typically 50m from the cryostat. Protection of the klystrons against excessive reflected power is proposed to be ensured by electronic safety systems inducing short interruptions of the RF power if the reflected power exceeds a threshold value, as demonstrated on the 3.7GHz klystrons of Tore Supra. Circulators may be used as on the 3.7GHz plant at JET, but require further development for use at 5GHz and 500kW CW.

It is proposed to use a single circular waveguide propagating the TE0,1 mode fed by a module of 6 klystrons to transmit the power to the launcher. This gives low losses and relative insensitivity to the loss of an individual klystron. Total losses over 50m are estimated to be below 0.3dB (7%). The circular mode TE0,1 can be excited by six rectangular-triangular tapers as indicated in fig.III.10. Such a configuration induces the required electromagnetic pattern in the full cross-section of the circular waveguide and consequently, offers a robust mode excitation.

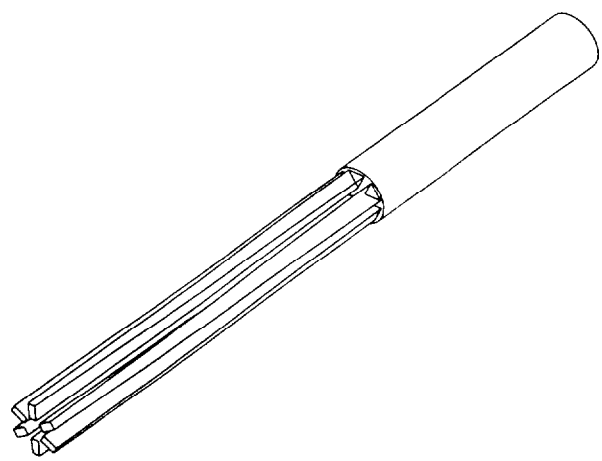

Fig. III.10 : The transition from six single mode guides to a single circular guide.

Further numerical calculations are required to fully describe the performances of such a circular hyperguide and its associated tapers, especially in case of fault regime (failure of an individual klystron, reflected power, etc).

Experience at JET and elsewhere with commercial beryllia pillbox windows at 3.7GHz indicates existing window technology to be capable of about 0.5MW per window at 5GHz. Basing the design on existing technology then requires the use of 6 windows for each module. Each incoming circular guide is thus divided back into 6 parallel single mode guides with discrete windows for the transition through the vacuum boundary. Inside the vacuum system, each of the six guides is coupled to the mode convertors at the excitor plane of the hyperguide. The overall conceptual assembly for one module from circular waveguide to grill mouth has been illustrated in fig.III.8 above.

It is envisaged to mount the six windows into a single remotely handleable module for assembly/removal from the vacuum vessel. The windows are located outside the cryostat where the neutron fluence will be below the 10^{22} /m^2 threshold at which degradation of the ceramic, in particular the loss tangent, becomes significant.

The windows are in turn connected to the hyperguide by single mode 53x24 mm waveguides. Flanges are incorporated in the single mode guides to enable the hyperguide/plug assembly to be removed horizontally independently of the incoming vertical waveguide assembly. The waveguides are manufactured in copper alloy with discrete stainless steel cooling tubes. These tubes access the vessel adjacent to the window module and allow the waveguides connected to the in-vessel flange to be removed vertically, either together with the window module or as a separate operation after removal of the windows. These waveguides are sufficiently flexible to accommodate differential thermal expansion betwen the waveguides and the vacuum vessel during baking of the waveguides/hyperguide for conditioning, as described below.

III.5.6. The Grill Support Assembly

It is necessary to provide a structure to support and locate the waveguide modules in the torus. The proposed design of this structure is illustrated in fig.III.11. It comprises a large egg-crate structure, incorporating eight ports for the eight plug assemblies, which locates off and is supported by the shield back plate. The design of the walls of this structure is similar to that of the shield cartridge, but of reduced width, and is illustrated in fig.III.12. The objective is for this support to form an integral part of the shield, in good electrical contact with the first wall. By this means, the slowly decaying currents flowing in the conducting first wall during a disruption also flow continuously across the grill, albeit in discrete conductors formed by the plasma facing surfaces of the egg crate. The decay time of this first wall current is typically 0.5s (determined by the first wall, not the launcher structure) which reduces eddy currents in the

structure behind the first wall to negligible levels. The first wall current itself only crosses the vertical field, producing a radially inwards pressure c.10 bar on the outer wall).

Each horizontal rail of the support carries typically 400kA, whilst the vertical rails may carry 150kA of halo current each. This gives rise to a radial load of typically 400 tonnes, which is essentially the same as would have appeared in the equivalent area of shield. This load is

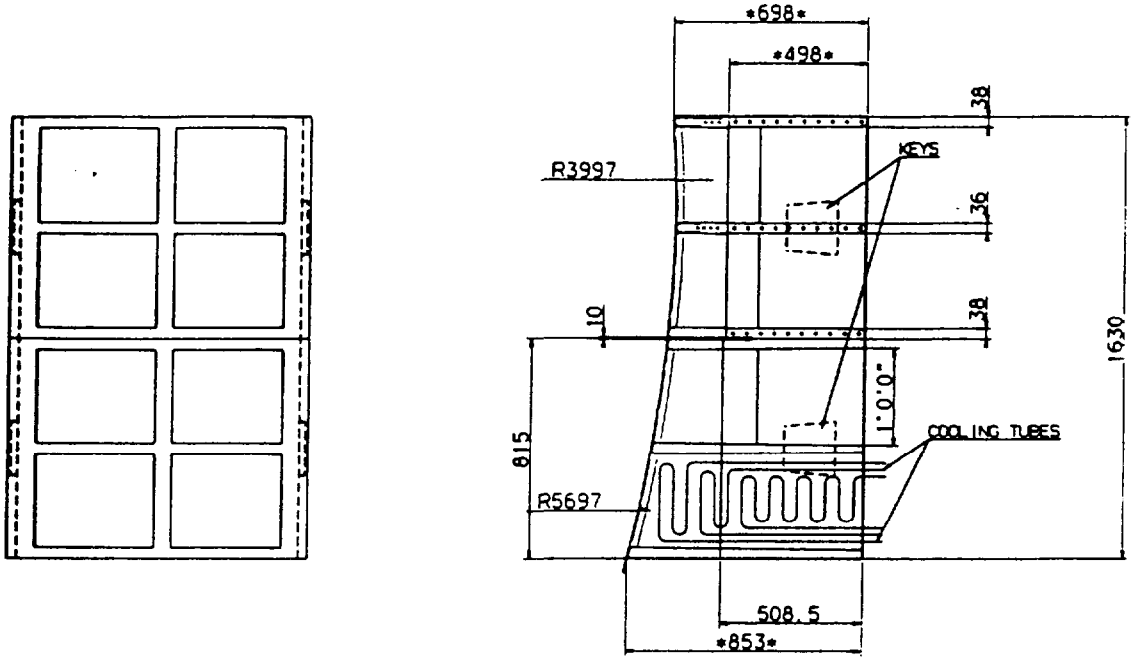

Fig. III.11 : The structure for supporting the grill in the port/first wall.

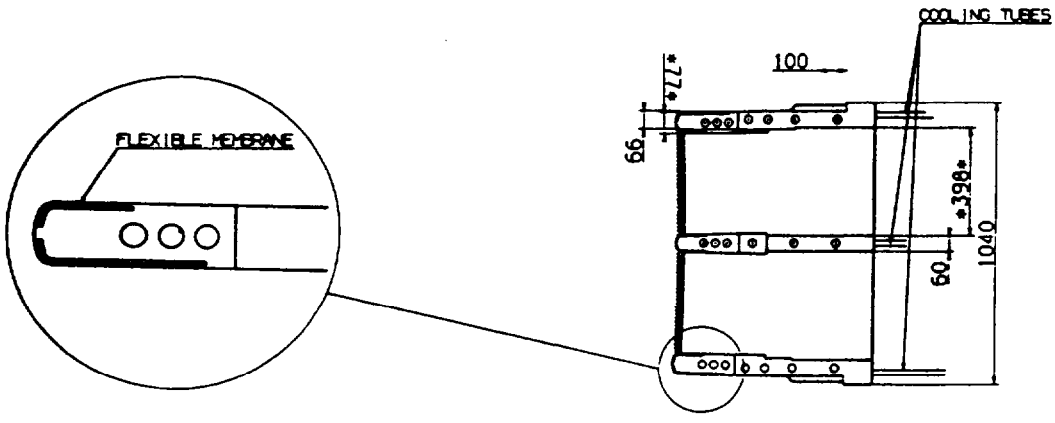

Fig. III.12 : A detail of the wall of the support structure.

carried by the shield backplate without undue stress except locally in the attachment of the launcher support to the backplate. This is conceived to be a key arrangement supporting both radial and shear loads on each of the four sides of the support assembly.

The segmentation of the current in the launcher support allows some fringing of the field between rails. This gives rise to circulating currents in the various walls both of the support and the plugs. These lead in turn to moments about the various axes, the dominant moment being about a radial axis. This moment has been estimated to be 100 tonne.m in total on the support, equivalent to a shear force of typically 50 tonnes on each of the four sides of the support.

The electrical contact with the shield is established via an inflatable membrane, as seen in the detail of fig.III.12, held in place by the coolant pressure. This feature is again similar to the principle of the shield cartridges. The membrane is stainless steel with copper cladding. A coating of beryllium is applied on the plasma facing surface.

Each plug is pressed into the support by a spring washer assembly located near the plane of the hyperguide excitor. The radial position is defined 250mm from the mouth by locating steps as shown in fig.III.11. The plug is located laterally by deformable membranes on the shield, which also establish electrical contact. The front 200mm of the support is tapered inwards, to match a similar taper on each plug. This accomodates swelling due to irradiation. This taper will not reverse under the anticipated swelling, which enables removal of the plug after irradiation. It may be necessary to shim replacement plugs to fit the swollen support. The support is split at the horizontal centreline to enable accommodation at this split of half of the swelling in the vertical direction. The support itself must be sized relative to the hole in the backplate and the port to accommodate typically 10mm swelling in outside dimensions in both the horizontal and vertical directions, tapering to zero over the front 200mm.

Cooling of the support is by discrete cooling tubes embedded in the structure. The front 300mm is anticipated to be copper alloy with stainless steel tubes; the rear part may be all stainless steel. Many parallel cooling channels with few in-vessel welds are foreseen. These will penetrate the vacuum boundary at the end port of the vacuum vessel outside the cryostat (see fig.III.2). The complete support structure with cooling pipes may be installed and replaced remotely through this port.

III.5.7. Vacuum Vessel

The ITER vacuum vessel is required to be designed in accordance with the ASME VIII code for 20 bar internal pressure. The outline design of the launcher vessel has been carried out broadly in accordance with Part 1 of the code. In some cases, notably the use of lip welds for remote handling, full analysis in accordance with Part 2 of the code will be required. Such analysis has not been carried out at this stage. The material is stainless steel 316.

Thus, for example, the main vessel which is of 2.2m diameter has 30mm wall and a heavily re-inforced end flange for connection to the torus port. The vessel runs through the cryostat into a cave where assembly/dis-assembly of all internal components takes place. The vessel is connected to the cryostat by a double bellows able to support the internal 6 bar pressure in the cryostat and maintain the integrity of the cryostat. The vessel is rigidly attached to the torus port via a pancake which is used to supply services to the lower shield module. A layout of the vessel is seen in fig.III.2.

Additional neutron shielding is incorporated both around the vessel and inside the vessel in the cryostat penetration to reduce the neutron flux into the cave. Detailed numerical modelling of the residual flux at the windows has not been carried out. If necessary, further passively cooled shielding may be conveniently added in the cave in the horizontal plane of the internal waveguide flanges to protect the windows.

Outside the cryostat, the vessel has a 3.4m diameter side port for connection of the RF windows, a 0.6m diameter port for vacuum pumping, and a main end-port which gives access for installation of in-vessel components and carries the services to these components. The vessel is supported at the centre-of-mass on a sprung bogey which allows radial movement during baking, and which can be adjusted to the correct height on compliant springs, thus avoiding a significant bending moment appearing on the port flange.

The overall mass of the system is estimated to be 100 tonnes, largely in the vacuum vessel as shown in the breakdown of table III.4.

Component	Mass (tonnes)
Vacuum vessel	70
Support	5
Plugs	5
Waveguides/hyperguides	8
Bellows	10
Total	98

Table III.4. Masses of main sub-assemblies of the launcher.

III.5.8. Cooling and Baking Systems

The launcher is subject to large power inputs from neutron irradiation, plasma radiation and RF dissipation. These are summarised in table III.5. This demands active cooling of both the plug and the support assembly. Control of the dimensions of the hyperguide and mode convertors also requires these to be actively cooled. The ceramic windows must also be cooled for essentially steady state operation.

It is proposed to use the standard ITER cooling water for all systems on the launcher. The total dissipation of 4.3MW requires a total water flow rate of 140m^3/hour with a temperature rise of 30C. The inlet temperature will be 150C and exit temperature 180C, except for the hyperguides/mode convertors where the temperature rise is limited to 10C for dimensional control. Flow rates through the various subsystems are summarised in the table III.5.

The vacuum vessel will be heated during normal operation to 150C using the same cooling water system with an estimated power requirment of 100kW and flow rate of 10m^3/hr and 10C differential temperature.

	Support	Plugs/ hyperguides	Waveguides	Windows
Neutron power dissipation (MW)*	0.66	1.7	0	0
Plasma radiation (MW)**	0.22	0.56	0	0
RF losses (MW)	0	0.55	0.4	0.17#
Total dissipation (MW)	0.88	0.8	0.4	0.17
Water inlet temperature (C)	150	150	150	150
Water exit temperature (C)	180	180	180	160
Water flow (m3/hour)	24	80	11	14

Table III.5. Main parameters of the launcher cooling system
(* at 1.5MW/m^2; ** at 0.5MW/m^2; # 0.04 dB)

Experience on existing lower hybrid systems has shown conditioning of the waveguides in vacuum to be strongly enhanced by baking to a temperature more than 50C above normal operating temperature. It is therefore envisaged that all waveguides in vacuum, including in particular the plugs, are bakeable to 250C independently of the torus temperature. Differencial expansion in length between the RF systems and the vacuum vessel of typically 10mm is accommodated by bending of the incoming waveguides inside the vessel. Differential expansion of 0.5mm between the plugs and the support is accommodated on the deforming membranes. This baking will be achieved by blowing nitrogen at 250C, 20 bar through the relevant water cooling channels. A power of c. 75kW would give a rise time from 150 to 250C of 3 hours and sustain the radiation losses on the plugs at 250C for an emissivity up to 0.25. The required flow rate for a 30C temperature differential is 450m^3/hr. The Reynolds number of the nitrogen flow is then close to that of the water flow through the same tubes, and the pressure drop is thus about 2 bars. The main parameters of the baking system are summarised in table III.6.

It is noted that an alternative to nitrogen is the use of steam for baking. This would require a much smaller pump (20m^3/hr liquid), but would also require a 260C steam generator, a 200C condenser and a regenerating heat exchanger.

Internal components	
Fluid	Nitrogen
Inlet pressure	20 bar
Exit pressure	18 bar
Inlet temperature	260C
Exit temperature	240C
Flow rate	$450m^3/hr$
Vacuum vessel	
Fluid	Water
Inlet pressure	20 bar
Exit preesure	15 bar
Inlet temperature	150C
Exit temperature	140C
Flow rate	$10m^3/hr$

Table III.6. Main parameters of the launcher baking system

III.5.9. Pumping system

During RF operation, and particularly during conditioning, there is substantial outgassing from the surfaces of the waveguides. This leads to an increase in pressure in the waveguides. Experience shows that breakdown occurs if the pressure increases above typically 10^{-4} mbar. Maintaining the pressure below this level requires the provision of additional pumping systems on the launcher, combined with adequate conductance both along and into the waveguides.

The outgassing rate found on well-conditioned present generation systems is 10^{-6} Pa.m/s [22-24]. The surface area of the proposed launcher exposed to RF is c.300 m^2, which gives a total outgassing rate of $3x10^{-3}$ mbar.l/s. At a background pressure in the launcher vessel of 10^{-6} mbar, the required pumping speed is 3000 l/s. An order of magnitude larger pumping speed can be readily achieved with a 1 m diameter liquid helium cryopump located outside of the cryostat. This pump will require occasional re-generation into the torus, typically every few burn hours. An outgassing rate two orders of magnitude higher can be tolerated during long pulse conditioning, and short pulse conditioning will accept a further several orders of magnitude higher outgassing rate.

III.5.10. Remote Maintenance

It is envisaged that the operations listed in Table III.7 would be performed remotely :

Operation	Location	Planned	Frequency
Replacement of plug/grill mouth	Ex-cryostat	Yes	1000 burn hours
Replacement of support	Ex-cryostat	No	Few times in total
Replacement of window module	Ex-cryostat	Yes	1000 burn hours
Replacement of mode convertor	Ex-cryostat	No	Few times in total
Replacement of lower shield module	In-cryostat	No	Unknown

Table III.7. Remote handling operations on the launcher.

Those operations indicated as 'planned' are expected to have to be done at regular intervals as a consequence of the design. Other operations are possible remotely but would only be carried out if required to recover from a failure. All operations are carried out in the ex-cryostat cave, apart from replacement of the lower shield module which requires the launcher vessel to be removed from the port.

All cooling pipework is envisaged to be removed/installed as an integral part of the component being supplied, thus avoiding in-vessel remote welds of cooling pipes.

IV. RESEARCH AND DEVELOPMENT

IV.1. Physics R&D Requirements

IV.1.1. Code Development

Further validation of the Lower Hybrid codes on experimental data closer to ITER parameters is required. Wave propagation and absorption need to be studied especially for conditions of off-axis deposition in H-mode and VH-mode plasmas.

IV.1.2. MHD-Stability

The MHD stability of hollow current profiles has to be assessed in experiments with high-β_p plasmas.

IV.1.3. Current Profile Control

Full control of the plasma current profile has to be demonstrated in high-β_p tokamak discharges. Current profile feedback control has to be developed. This requires the development

of appropriate current profile diagnostics to routine operation and the development of feedback control systems acting simultaneously on central and off-axis current drive.

IV.1.4. Transport Model

A local transport model for H- and VH-modes has to be developed and validated on experimental data.

IV.2. R&D Programme Required for the Launcher

The design of the launcher has been largely based on existing technology. However, a number of novel features require further development. In addition, some critical aspects of the interaction between the plasma and the launcher require better understanding. The requirements for further development are as follows :

IV.2.1. Study of erosion and redeposition

Erosion/re-deposition of the proposed plasma facing materials (in particular Be) need to be assessed. The uniformity, the rates of erosion/re-deposition and the physical properties of redeposited material need to be studied.

IV.2.2. Study of active coupling control

The control of good coupling of LH waves with low reflection at large plasma-launcher distance needs further studies, especially in long pulse operation with H-modes. An extension of the existing coupling codes (e.g. SWAN) to more generalised geometries and the active-passive waveguide array is required.

IV.2.3. Tests of the Hyperguide

Further testbed measurements and experiments on plasma are required in order to assess the transmission properties under mechanical deformations and with varying reflection coefficients on the receiver side. The existing Hypercode has to be extended to more generalised geometries.

IV.2.4. Tests of the microwave components

The following microwave components need to be built and tested :

- Mode converters for the conditions of the proposed ITER launcher.
- A window for 0.5MW at 5GHz, to sustain 20 bar internal pressure.

- The power splitters and combiners at the transition between standard size and circular waveguides in the transmission lines.

IV.2.5. Development and tests of a klystron

A klystron for 0.5 -1 MW/CW at 5GHz has to be developed and tested.

IV.2.6. Tests of an integrated launcher module

A complete module, comprising mode converter, hyperguide and active-passive grill coupler, has to be built and tested on plasma. This could be done also at a different frequency with systems existing on present day machines. The LH systems on JET and TORE SUPRA would be especially suited because of their long pulse 3.7GHz capability. On TORE SUPRA the experiment would be performed for very long pulses, and this would lead to a test of a complete 3.7GHz module, compatible with the size of the machine ports. JET provides the additional feature of operation with divertor plasmas in H-modes which is essential for the assessment of reliable coupling and erosion effects caused by ELM´s.

V. SUMMARY

1. Operation Scenarios

The goals of ITER are the demonstration of ignition in pulsed and steady-state operation in an ignited state with control of the fusion burn. Non-inductive current drive and profile control are required both for long pulse and steady-state operation [1].

Full current drive and profile control on ITER can be most efficiently obtained with a combination of bootstrap current and Lower Hybrid Current Drive (LHCD) together with a seed current in the plasma center generated, if necessary by Fast Wave Current Drive (FWCD) or NBI-CD. LHCD has by far the highest current drive efficiency obtained in experiments and a broad data base exists [2].

Two scenarios have been studied in greater detail. In the standard ITER case with pulsed operation at a plasma current of 25 MA, LHCD can provide sawtooth control. In an advanced scenario of steady-state operation with non-monotonic q profiles, LHCD is used to create deep shear reversal and to provide full current drive together with the bootstrap current [3]. In both cases off-axis noninductive current drive is required. This is naturally obtained with LHCD at high electron temperatures, in excess of 10keV. The required hollow current profile should be generated already during the early low-ß stage of the discharge in order to avoid passing through MHD-unstable configurations during high power heating and burn, and also because the (relatively) short resistive time in this stage allows to obtain the desired q-profile faster. It is important to note that LHCD will be the only efficient current drive method in this initial low temperature stage of the pulse. This type of advanced scenarios and the associated feedback loops will be tested on a smaller scale with the systems available on JET and TORE SUPRA.

Heating to ignition may be obtained with LHCD alone. A burn instability may develop in conditions where the local heat conductivity depends on the local q value. The resulting oscillations in the fusion power output can be stabilised by active current profile control with combined noninductive current drive by LHCD and FWCD. The simultaneous use of FWCD (or NBI-CD) for central current generation and LHCD for off-axis drive provides full control of the whole current profile. A consistent MHD-stable scenario is obtained at a plasma current of 13.5MA, with a bootstrap fraction I_{bs}/I_p~0.7, I_{LH}/I_p~0.2-0.25, I_{FW}/I_p~0.05-0.1. A fusion power output of order 1GW is produced in steady state.

Modelling of the ITER scenarios including heating and current drive by FW, NBI and LHW, has been performed both with the transport code JETTO and also independently with the 1-D transport code ASTRA in which the local Rebut-Lallia-Watkins heat diffusivity was used. The JETTO results are analysed with the MHD stability code CASTOR, to study the behaviour of ballooning, kink and infernal modes. Reliable modelling of LHCD can be performed now with codes validated on existing experimental results. Lower Hybrid power

and current deposition profiles in ITER were calculated within JETTO with a model based on a full wave solution [4]. This model had been validated on a wide range of tokamak discharges with LHCD on ASDEX [5] and JET. LH wave propagation and absorption were also separately calculated with the two stand-alone codes BARANOV and BANDIT3D. Parameter studies for LHCD application to ITER were performed with the two codes prior to scenario modelling in order to assess the appropriate wave frequency and the location of the launcher.

Feedback schemes which are necessary to control the discharge against non-linear interactions between external and bootstrap current generation, current diffusion, heat transport and α-particle heating, have been studied with a time-dependent 1-D code (CRONOS). Prescribed MHD-stable reversed current profiles can be obtained through simultaneous feedback on the LH and FW powers as well as on the primary flux during the current profile formation phase (< 100s). During a shorter second phase the plasma radius and density are increased and the total current and external power rise until a prescribed amount of fusion power is obtained. The long-term evolution of the safety factor on axis can be controlled through a real time estimation of the central ohmic current density.

2. Lower Hybrid Heating and Current Drive System

A frequency of 5GHz has been selected as the lowest possible frequency to avoid absorption by α-particles ; the optimum spectrum peaks at $N_{//}=2$. A design is proposed based on modular units of ~ 24MW generator power each (one module per horizontal port).

The plasma facing structure of the launcher (refered to as the 'plug') consists of a so-called 'reflector waveguide array' in which every second waveguide is a short passive one. This design allows provision of active cooling channels close to the waveguide apertures, and by using copper alloys or possibly berylium it permits cooling of the grill mouth by conduction under the intense ITER neutron flux and plasma radiation. The depth of these reflector waveguides which optimises the radiated spectrum is about 15mm for the proposed launcher; the average pitch between waveguides is 11.25mm. The length of the 'plug' (0.8m) accomodates built-in phase shifters and multijunction splitting networks to produce the required phase distribution (135°) with high directivity (85%) combined with low reflection (a few percent). A benefit of the proposed design is that the 'plug' is typically 60% dense and can therefore provide similar neutron shielding as the first wall shield modules. Electrical contact with the shield at the first wall level is insured.

The 'plug' in turn is powered by 'hyperguides' which offer low losses and excellent vacuum pumping. A total of eight 317x345mm hyperguides operating in the $TE_{0,6}$ mode conveniently fills the available area. Each of these modules corresponds to about 3 MW of generator power, provided by 6 klystrons of 0.5MW each with one vacuum window per

klystron, all based on present technology. Mode converters are used to couple the six incoming waveguides to the 'hyperguide'.

The launcher is enclosed within a vacuum vessel able to sustain an internal pressure of 20 bar (as does the torus vessel). The launcher vessel extends through the cryostat inside a double bellow able to maintain the cryostat internal pressure of 6 bars. The RF windows are placed outside the cryostat where the neutron flux is below the allowable flux for BeO windows.

Remote maintenance of the launcher is performed by exchanging, from outside the cryostat, the hyperguide/plug modules, or in the event of failure also their support structure. These modules may be re-furbished off-line if required.

The associated R & D programm is mainly dedicated to the development and tests of specific component as RF windows and klystrons working at 5 GHz and in the power range of 0.5 to 1MW. Moreover other novel components as mode convertor, hyperguide, passive-active grill, require further test bed measurements and experiment on plasma.

The test in present machine as Tore Supra or JET of a 3-4MW integrated launcher module working at 3.7GHz and comprising such novel components is strongly supported.

APPENDIX 1
LOWER HYBRID CODES

A.1.1. LH Wave Propagation

LH wave propagation and absorption were studied with the two stand-alone codes BARANOV and BANDIT3D [7]. Both codes include ray tracing and Fokker Planck calculations. The LH wave propagation is treated in a similar way in both codes. Different approaches are used to solve the Fokker-Planck equation in order to determine the electron distribution function. The electromagnetic part is included into the dispersion relation. The calculations are carried out in toroidal geometry, taking into account equilibrium magnetic field in the three moments approximation (i.e. Shafranov shift, elongation and triangularity).

The BARANOV code includes also the scattering of the slow LH waves by low frequency density fluctuations, using a theory proposed by E.Ott [8]. The spectrum of the fluctuations is approximated by a Gaussian function

$$S(k)=(1/\pi k_o^2)\langle \delta n/n\rangle^2 \exp(-(k/k_o)^2),$$

where k is the wave vector of the fluctuations. The characteristic wave scale length k_o^{-1} is assumed to be of the order of the ion Larmor radius ρ_i . The amplitude of the fluctuations is distributed in space according to:

$$\langle \delta n/n\rangle^2 = \Delta\rho\rho_i/a^2,$$

where ρ is the radial co-ordinate and a the minor radius. The parameter Δ is introduced to investigate the influence of the fluctuation amplitude on the distribution of the driven current. The best agreement between the experimental data and the results of the calculations is obtained for $0.25<\Delta<1$.

A.1.2. Fokker-Planck Calculations

BANDIT CODE : The relativistic 3D ($p_\perp$,$p_{//}$,r) Fokker-Planck equation is solved numerically. The Fokker-Planck equation includes neo-classical trapped particle effects and electron diffusion. For ITER calculations zero diffusion is adopted. This code should properly describe the influence of an electric field on the LH driven current and the runaway effect.

BARANOV CODE. There are two options for the calculation of the electron distribution function. It can be found via a numerical solution of either the relativistic 2-D ($p_{//}$-parallel momentum, r-radial coordinate) Fokker-Planck equation or the 2-D ($p_{//}$-parallel momentum, $p_\perp$-perpendicular momentum) Fokker-Planck equation.

a) 2-D ($p_{//}$-parallel momentum, r-radial co-ordinate) Fokker-Planck equation.

The radial diffusion is included. It is assumed that the diffusion of the fast electrons is connected with the stochasticity of the magnetic field. In the framework of this model

$$D_{\rho\rho} = D_m \, v_{//}/v_e ,$$

where $v_{//}$ is the parallel phase velocity and v_e the thermal electron velocity. A typical value of $D_m = 0.5$ m^2/s was chosen. The collision frequency is decreased by a factor of C_l=0.55 to reproduce the current drive efficiency derived from experimental results as well as the observed hard X-ray emission. It should be noted that from a comparison of two- and one-dimensional non relativistic calculations $C_l = 0.4$ [9].

It is assumed that the electron distribution function is spread in the perpendicular direction due to pitch angle scattering. In the plateau region and beyond, the characteristic perpendicular temperature is given by

$$T_\perp = C_2 E_\perp ((v-v_1)/(v_2-v_1))^2 \text{ for } v_1(\rho)<v<v_2(\rho)$$

and

$$T_\perp = C_2 E_\perp \text{ for } v>v_2,$$

where v_1 , v_2 are the lower and upper boundaries of the parallel phase velocity distribution of the LH waves and $E_\perp$ is defined in [10].

b) 2-D ($p_{//}$-parallel momentum, $p_\perp$-perpendicular momentum) Fokker-Planck equation.

The solution describes properly the quasi-linear diffusion in the presence of a small electric field, taking into account the pitch angle scattering of the fast electrons.

A comparison of the results calculated by the two different options shows that for a JET discharge with a central density $n_{eo}=3.5\text{x}10^{19}\text{m}^{-3}$ and the central electron temperature T_{eo}=19keV at 6 MW of LH power the calculated driven current profiles are similar to each other. There is 6% difference in the calculated efficiencies. Simulations of ITER discharges show a larger discrepancy between the results obtained with the two different Fokker-Planck equations. For an ITER model case with $n_{eo}=1.24\text{x}10^{20}\text{m}^{-3}$ and T_{eo}=15 keV at 50MW of LH power the calculated LH driven current is a factor 1.42 higher with the option b.

A.1.3. Code Validation

The BARANOV code had been validated previously upon Lower Hybrid current drive experiments on JET [11]. The parameters for the amplitude of the density fluctuations and the fast electron diffusion were determined from a comparison of code calculations with the

measured profiles of fast electron density and temperature and the total LH driven current. A large number of discharges in a wide range of densities and LH power could then be modelled without any further adjustment of code parameters. The BANDIT3D code was cross-checked against the BARANOV code with runs for the same model cases. The model developed by Pereverzev [4] was validated on LHCD discharges with a wide parameter range on ASDEX [5] and on the JET discharges which were modelled also with the BARANOV code.

APPENDIX 2
COUPLING OF LH WAVES AT LARGE PLASMA-LAUNCHER DISTANCE

The Lower Hybrid launcher proposed in this report for ITER will stay embedded in the first wall at a fixed position during plasma operation. The option of radial movements has been discarded in order to protect the front end structure against excessive heat deposition. The plasma position may still be adjusted to meet the coupling requirements. However, a large clearance between the separatrix and the first wall has to be maintained in order to keep erosion at an acceptable level. H-modes also require a separatrix-wall distance of at least 3-5 density decay lengths.

Good coupling of Lower Hybrid waves to plasmas with large distance between the last closed flux surface and the front of the LH launcher has been obtained for divertor plasmas in ASDEX [25] and JT`60U [26] and for limiter plasmas in TORE SUPRA [27].

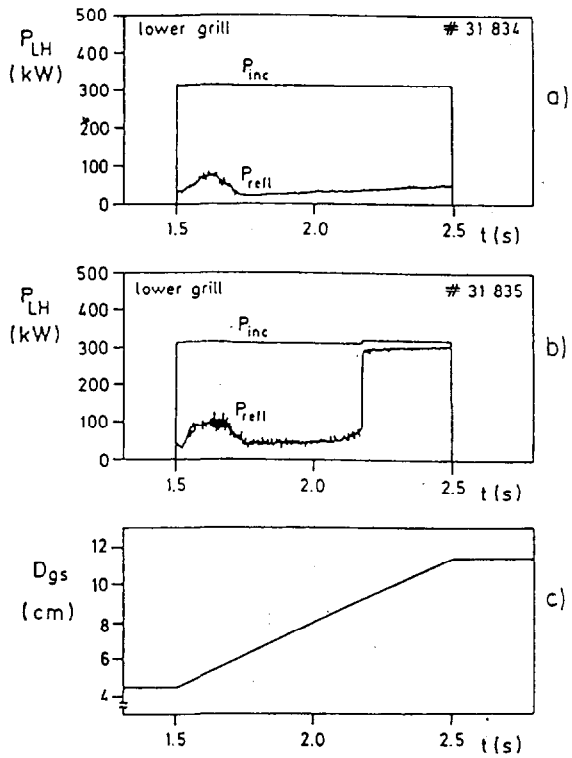

Fig. A2-1 : Variation of the average reflection coefficient <R> while the plasma is moved away from the grill.

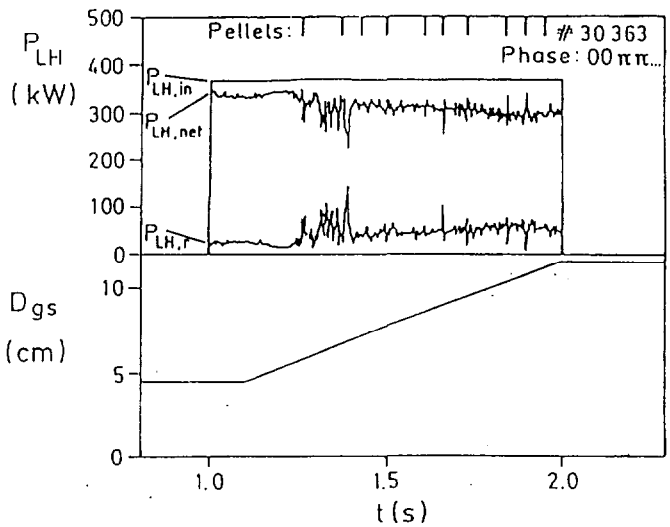

Fig. A2-2 : Incident, net and reflected rf power as a function of time while the plasma is moved away from the grill with simultaneous pellet injection.

In ASDEX, low reflection could be maintained when shifting the plasma radially off the launcher up to a distance of 10cm. Larger clearances could be sustained by using a gas feed near the LH launcher (Fig. A2-1). With shallow pellet fuelling even larger distances up to 11.5cm were achieved at low reflection (Fig. A2-2). The current drive efficiency was not

affected in all these cases. In JT-60U, good coupling was obtained with a distance of 20cm between the plasma and the LH grill located in a lower port in front of a plasma region with a wide scrape-off layer. In TORE SUPRA, experiments with radial displacements of the LH

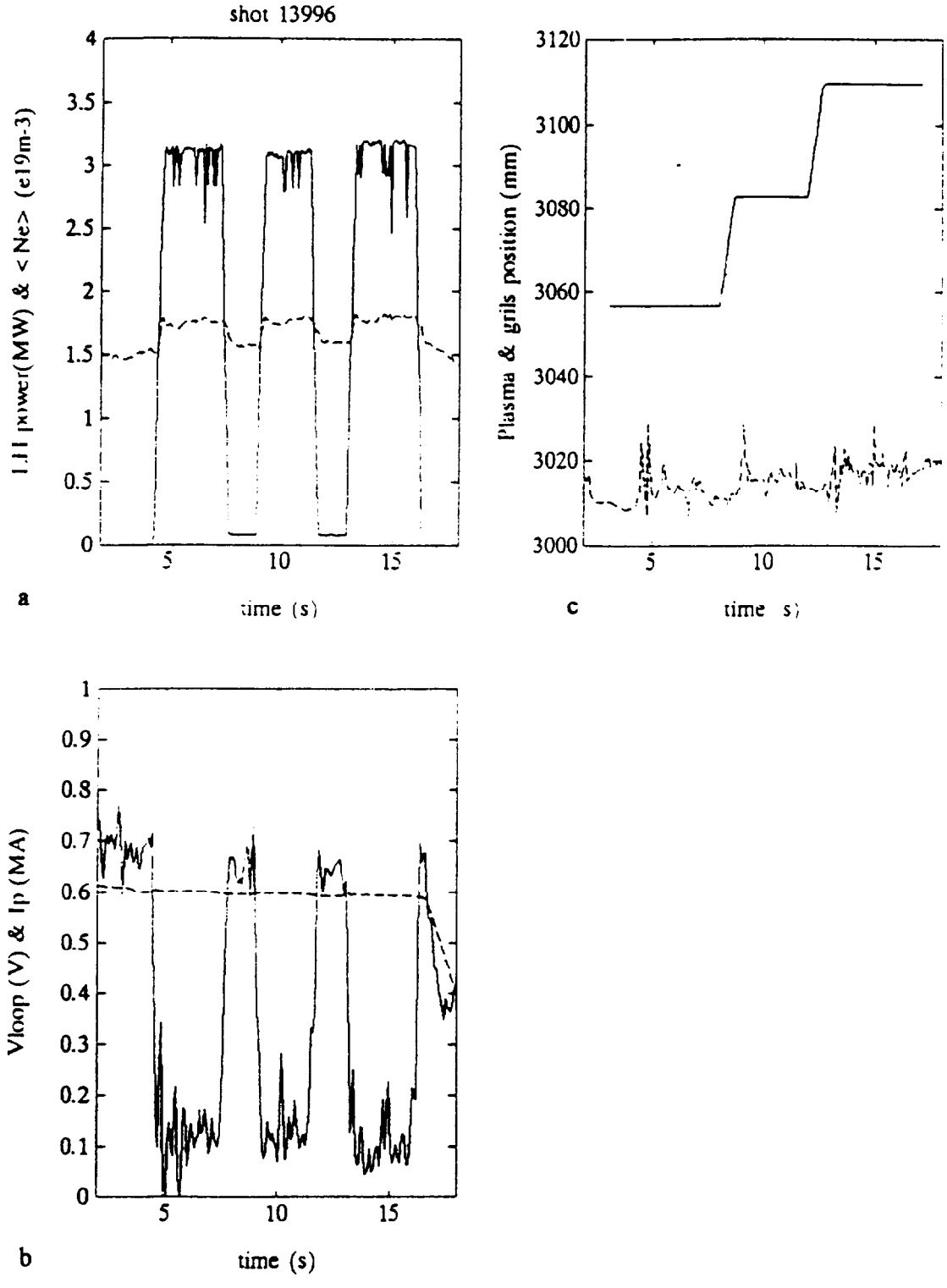

Fig. A2-3 : The RF driven current is not affected by the plasma grill distance.

launcher up to 10 cm during plasma discharges showed also that good coupling can be maintained at large plasma-grill clearance. High power results are shown in Fig. A2-3 for a case with three LH pulses into a plasma discharge at three different grill positions, as seen in Fig. A2-3(c). The power transmission through the plasma edge layer is the same in all conditions, as seen from the same level of loop voltage reduction in Fig. A2-3(b). In JET, first experiments with LH in the new divertor machine configuration showed also remarkable insensitivity of the coupling to plasma displacements of up to 6cm during LH application. Gas puffing near the grill improves coupling. Good coupling could be maintained also during ELMy H-modes.

Coupling code calculations for the active-passive waveguide structure proposed for the ITER launcher give a wide density range for operation at low reflection, as discussed in Appendix 3. Reflection coefficients below 5% can be expected with realistic density gradients and a density of $6x10^{17}m^{-3}$ in front of the grill. This should allow a plasma-grill distance of order 15cm.

APPENDIX 3
PASSIVE/ACTIVE WAVEGUIDE ANTENNA

This new concept of antenna which has been first described by [16] uses a juxtaposition of active and passive waveguides. Then the passive waveguide depth is adjusted in such a way that the total electric field in the passive waveguide is coherent in amplitude and phase with the field in the active ones. The result is then that the coupling and the directivity properties of the radiated N// spectra are similar to those of more classical LHCD antennae.The total electric field E in the passive waveguide mainly depends on :

- the cross coupling coefficient, S_{12} , through the plasma between active and passive waveguides,
- the phase shift between active waveguides, 2φ.
- the passive waveguide depth, lcc.

It is given by the following relation where λ is the vacuum wavelength :

$$E = 2S_{12}e^{j\varphi}\cos\varphi[1+e^{j\pi(1-4\frac{lcc}{\lambda})}]$$

The main peaks in the radiated $N_{//}$ spectrum are situated at the different positions $N_{//n}$ when the active waveguides are fed independently. The values are given by the relation

$$N_{//n} = \frac{\varphi}{k\Delta} + n\frac{\pi}{k\Delta}$$

where and k are the toroidal geometric period and the vacuum wavenumber respectively.

To study this new antenna, computations have been made using the SWAN code, simulating nine active waveguides fed independently and ten passive waveguides. Two evanescent modes have been taken into account for boundary conditions at the plasma antenna interface. The geometric period and phase shift have been adjusted in such a way

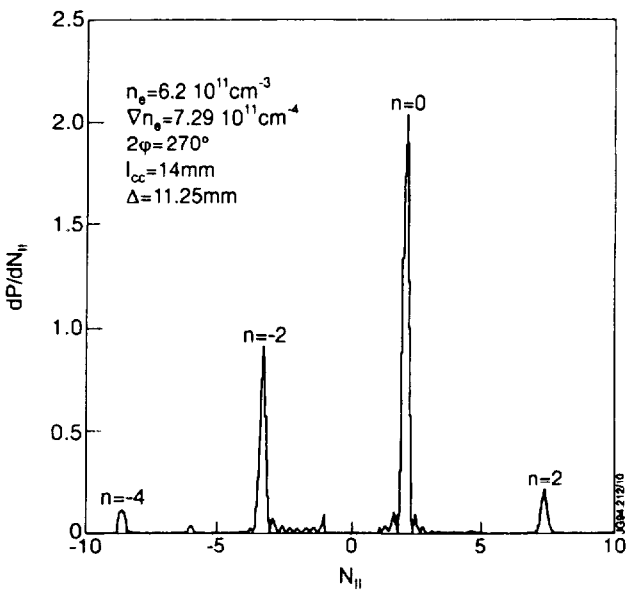

Fig. A3-1 : The computed spectrum for the proposed active/passive grill.

as to have a main peak in the radiated spectrum at $N_{//}=2$. In Fig A3-1 an example of the $N_{//}$ spectrum is given showing that the radiated spectrum is similar to the one of classical antenna. The peaks corresponding to an odd indices have been removed by the coherence between active and passive waveguides.

The mean reflection coefficient R, the power directivity D, and the $N_{//}$-weighted low temperature current drive efficiency η^*, are taken as defined in [28]. The dependence of each of these parameters on the electron density, the electron density gradient, the phase shift between active waveguides, the passive waveguide depth and the thickness of the wall has been studied.

a) Dependence on the electron density

The computation has been made with an electron density gradient of $7.3 \times 10^{11} cm^{-4}$, a passive waveguide depth of 12mm and two different values for the geometric periodicity : 10mm, for which the phase shift between active waveguides is 240°, and 11.25mm, for which the phase shift is 270°. The mean reflection coefficient are given on Fig A3-2 and the power directivity and current drive efficiency in Fig. A3-3. Two features are noted :

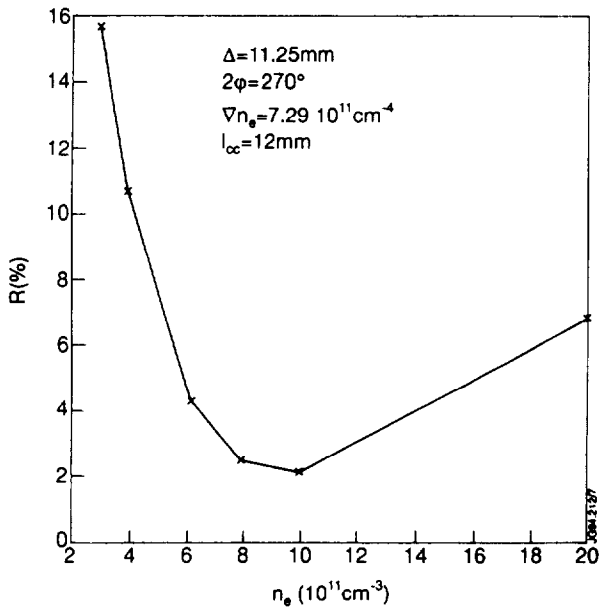

Fig. A3-2 : Dependence of reflection on electron density.

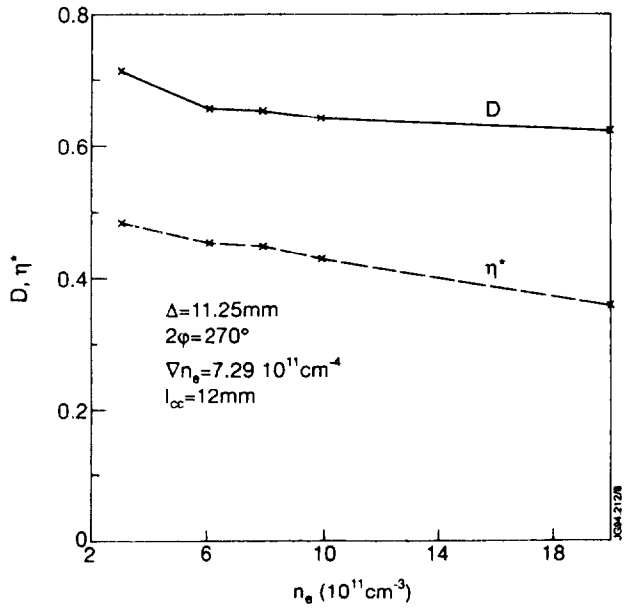

Fig. A3-3 : Dependence of directivity and current drive efficiency on electron density.

First, the coupling is lowest at three times the cut-off density but even at the cut-off density the reflection coefficient is still lower than 16% due to the change of the cross coupling coefficient S_{12} and the distance between active waveguides.

Secondly, the directivity is smoothly decreasing when the density is increasing. The current drive efficiency at the $N_{//}$ value of 2 is higher for a phase shift of 270° and a geometric

period of 11.25mm due to the suppression of the peak on the $N_{//}$ spectra corresponding to the index n=-1.

Consequently, this antenna can work quite far from the plasma where the heat flux is lower.

b) Dependence on the electron density gradient

Keeping the electron density constant at $6.2x10^{11}cm^{-3}$, the density gradient has been changed from 3 to $13x10^{11}cm^{-4}$, corresponding to a decay length changing from 20 mm to 5mm.

In the range of the density gradient of 6 to $12x10^{11}cm^{-11}$, the reflection coefficient remains below 3% while power directivity and current drive efficiency are almost constant, as shown in Figs A3-4 and A3-5.

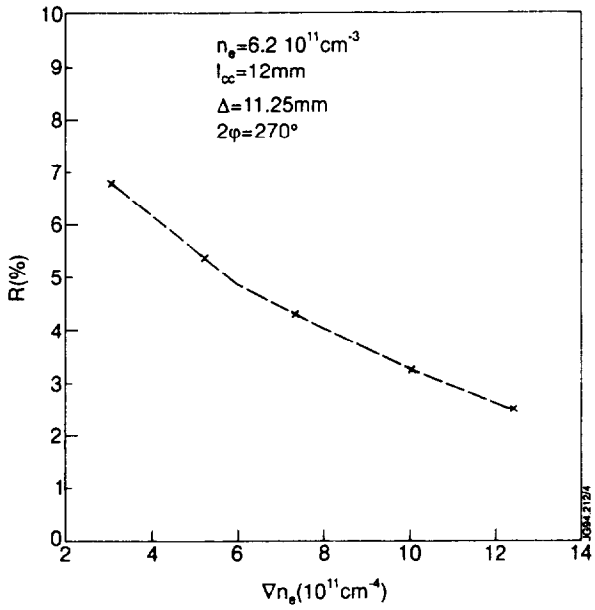

Fig. A3-4 : Dependence of reflectivity on electron density gradient.

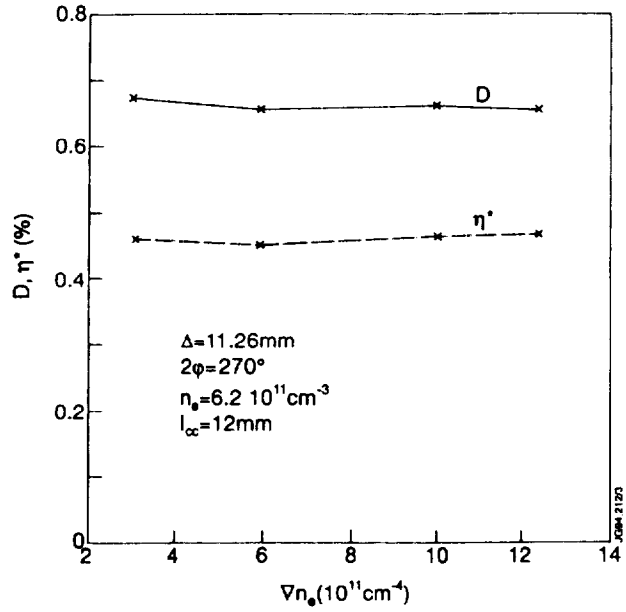

Fig. A3-5 : Dependence of directivity and current drive efficiency on electron density gradient.

c) Dependence on the active waveguide phase shift

This has been studied for an electron density twice the cut-off density, an electron density gradient of $7.3x10^{11}$ cm^{-4} for two values of the geometric periods and for two values of the passive waveguides depth.

It is shown in Fig A3-6 that the mean reflection coefficient is lower for a phase shift of 240° when the passive waveguide depth is 12mm. For a passive waveguide depth of 16mm, it is less than 1% at 270°.

The power directivity changes with the geometric period and with the passive waveguide depth are small (Fig A3-7). The variation of the current drive efficiency is stronger, depending

on the cancellation (or not) of the peak near the $N_{//}$ value of -1. For the phase shift of 180 and 360°, the current drive efficiency is zero since the $N_{//}$ spectrum is then symmetric.

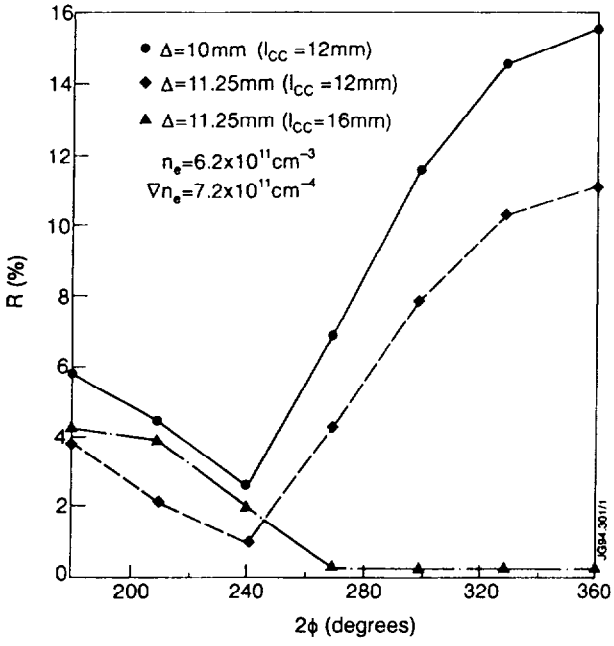

Fig. A3-6 : Dependence of reflectivity on the active waveguide phase shift.

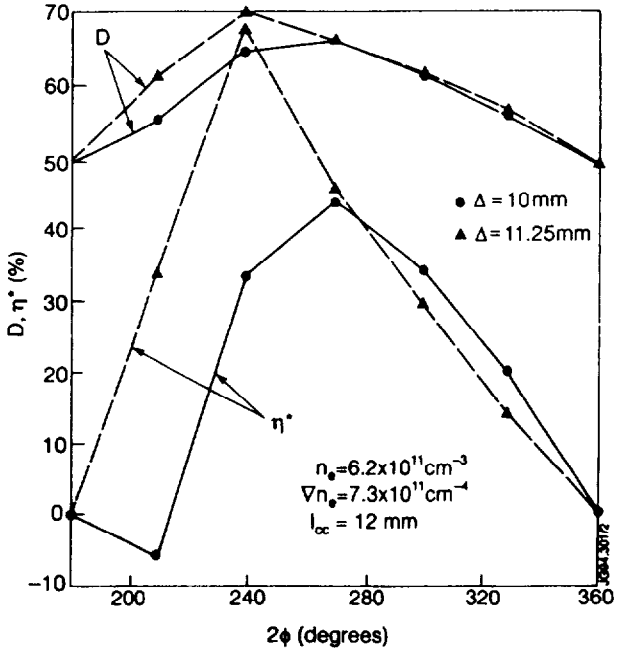

Fig. A3-7 : Dependence of directivity and current drive efficiency on the active waveguide phase shift.

d) Dependence of the passive waveguide depth

The only geometrical parameter available to adjust the coherence between active and passive waveguides is the passive waveguide depth. The effect of its variation has been studied. The calculations have been done at a density of twice the cut-off electron density and at a density gradient of 7.29x10^{11}cm^{-4}. This has also been done for two values of the geometric period and phase shift between active waveguides. It appears that the mean reflection coefficient is not sensitive to l_{cc} when the geometric period is 10mm but varies strongly with l_{cc} when it is 11.25 mm (Fig A3-8). But for this value the reflection coefficient is less than 2% on a range larger than 3mm.

On the other hand, the power directivity is unsensitive to l_{cc} with a geometric period of 11.25mm and varies more rapidly with a period of 10 mm (Fig A3-9). But where the change is the largest is on the current drive efficiency where the obtained value are higher for a geometric period of 11.25mm. The optimum value for geometric period of 11.15mm and a phase shift of 270° seems to be 16mm.

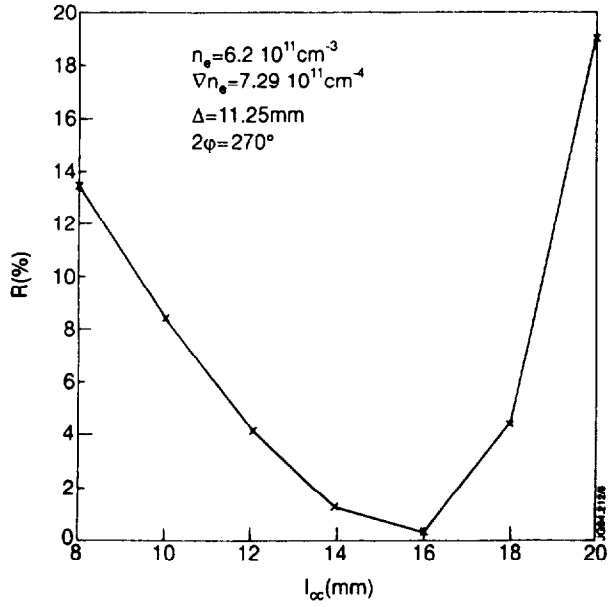

Fig. A3-8 : Dependence of reflectivity on passive waveguide depth.

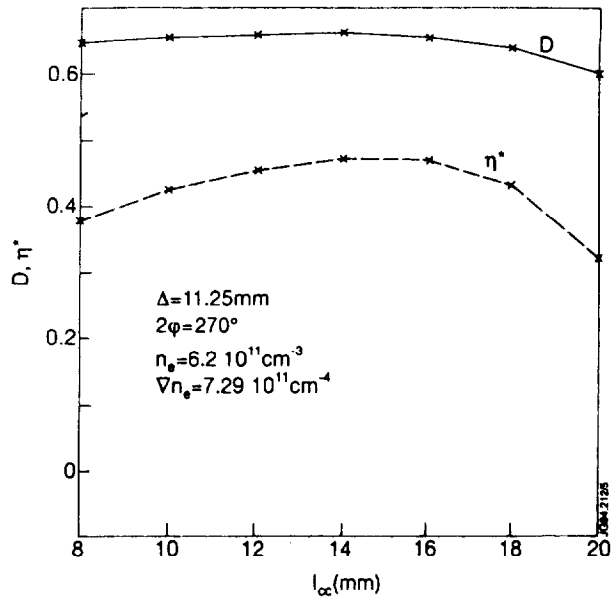

Fig. A3-9 : Dependence of directivity and current drive efficiency on passive waveguide depth.

e) Dependence on the wall thickness

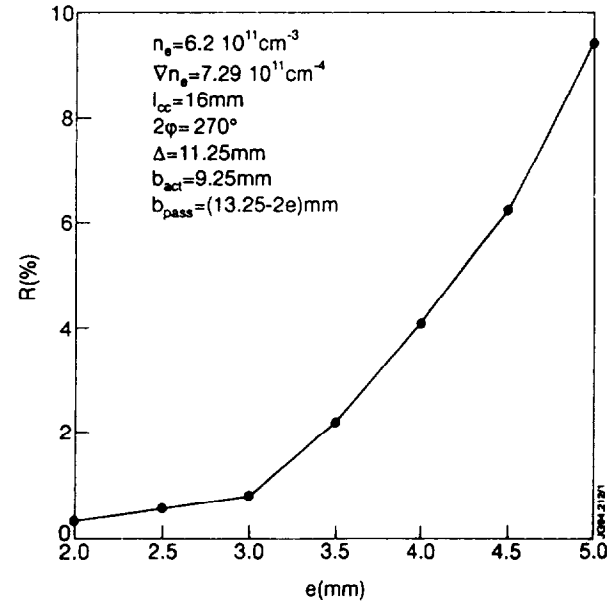

Fig. A3-10 : Dependence of reflectivity on wall thickness.

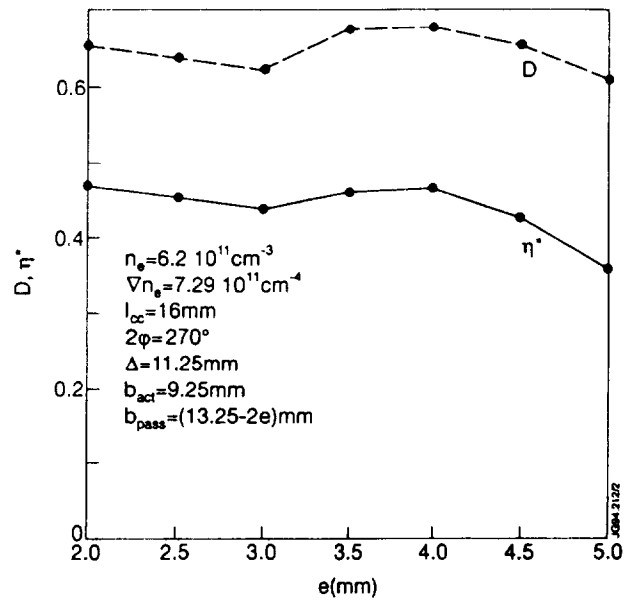

Fig. A3-11 : Dependence of directivity and current drive efficiency on wall thickness.

Due to erosion, a thickness of the wall of 2mm seems to be insufficient. So the effect of the change of this parameter on the coupling and on the radiated spectra has been studied. The width of the active waveguides has been kept constant at 9.25mm. A change of the thickness of

the wall leads to a decrease of the passive waveguides width. The study is performed for an electron density twice the cut-off density and an electron density gradient of $7.3 \times 10^{11} cm^{-4}$.

It appears that the mean reflection coefficient is increasing with the thickness of the wall. This is explained by a reduction in the cross coupling coefficient S_{12}. It reaches a value higher than 1% for a thickness larger than 3mm (Fig A3-10). The variation of the power directivity and the current drive efficiency is small (Fig A3-11).

APPENDIX 4
ITER HYPERGUIDE SIMULATIONS

A.4.1. The Hyperguide Concept

A conventional LHCD system for next step machines like ITER would require a launcher made of thousands of reduced waveguides facing the plasma. Conventional launchers using multijunctions become clearly unpractical as for instance the gas accumulation inside the launcher will limit the power handling capabilities of the antenna. As the front of the antenna is also the front piece of the multijunctions, this arrangement is not realistic in a reactor, where the need to replace the mouth because of plasma erosion will arise. A new design concept called Hyperguide has been developed in order to overcome these limitations. The Hyperguide structure is much lighter, simpler and cheaper to manufacture.

The Hyperguide is an overmoded waveguide providing near total power transmission between an emitter plate,fed by standard waveguides operating at the fundamental TE_{01} mode or mode converters operating at TE_{0m}, and a receiver providing the slow wave launching structure facing the plasma. The main propagating mode in the Hyperguide is TE_{0n} where N=mn with n the number of waveguide rows emitting a TE_{0m}.

A.4.2. Introduction to the Hypercode

A code, based on mode matching at the emitter-hyperguide and hyperguide-receiver interfaces, has been developed to calculate the wave propagation inside the hyperguide cavity. Up to 12 rows and 8 columns of waveguides can be used at the emitter and 12 rows and 32 reduced waveguides in the receiver. The code takes into account up to 6 modes in each of the emitter and grill waveguides and up to 200 in the hyperguide for both TE and TM modes.

Only straight waveguides can be modelled (no taper nor bend possible) and the walls of the emitter and grill facing the hyperguide are flat (no rounding nor taper possible).

The hypercode results have been validated by comparison with experimental results obtained with the Hyperguide prototype testbed in JET, which is a low power version of a full scale Hyperguide considered to be used on JET. Good agreement has been obtained for various scenarios with homogeneous and hetrogeneous power distribution at the emitter plate feeding the hyperguide.

A.4.3. ITER simulations

Several simulations have been done to estimate the power transmission and mode purity in an Hyperguide to be used in the LHCD Launcher on ITER.

The proposed ITER Launcher consists of 8 hyperguides assembled in 2 columns and 4 rows, each of 373x346 mm inner cross-section. Each hyperguide is fed by 6 mode converters through 6 vacuum windows. The length of the mode converters is 1500mm and the length of the hyperguide is around 7800mm. The grill mouth on the receiver side is made of 16 active and 17 passive waveguides split in 6 rows via step phase shifters. The width of the active waveguide is 9.25mm and the wall thickness between adjacent active guides is 13.25mm. The power coming from the hyperguide is split inside the reduced waveguides by a multijunction type E-plane junction.

Hyperguide:

For the purpose of the simulation, the characteristics of one hyperguide are as follows :

Frequency :	5 GHz
Inner cross section:	370x370 mm
Length:	3 m

Emitter:

Three different emitters to feed the hyperguide were considered. The first one is made of 3 rows and 2 columns of waveguides feeding the hyperguide with a TE_{02} mode.The second one is made of 2 rows and 3 columns waveguides each emitting a TE_{03} mode (see figure A4-1). The third one is made of 2 rows by 4 columns of waveguides each emitting a TE_{03} mode. In view of the present results the second type of emitter was selected.

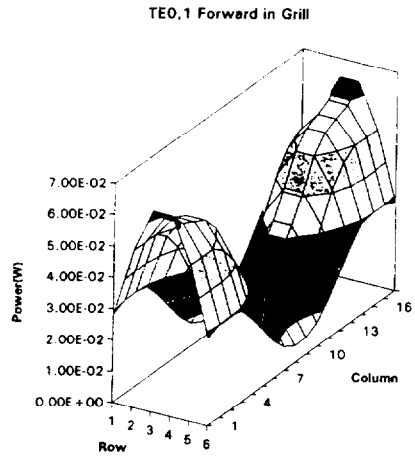

Fig. A4-1 : ITER Hyperguide case 2 (d).

Grill:

For the purpose of the simulation three square grills of 6x6, 6x18 and 6x4 waveguides were considered. The last type is selected. Each of the four waveguides is then further split into four reduced waveguides by a multijunction type of splitting network in order to generate a 180 degree phasing between the reflected power arriving back at adjacent waveguides, giving minimum reflection to the hyperguide.

A.4.4. Results

Results are tabulated in tables A4-1 and A4-2 for the following cases:

Case 1: Emitter with 3 rows and 2 columns

Waveguide dimensions in emitter :	181x119.3mm with 2mm wall
Input Power :	TE_{02} at 1 W and 0 phasing between rows.
Grill :	6x6 waveguide sizes 49.1x49.1 with 6.3mm wall

Case 2: Emitter with 2 rows and 3 columns

Waveguide dimensions in emitter :	119.3x181mm with 2mm wall
Input Power :	TE_{03} at 1W and phasing between rows.

Case 2a: Grill made of 6x6 waveguides

Case 2b: Grill made of 6x18 waveguides size 8x49.1mm

Case 2c: As Case 2a with emitter made with wall of 0.5mm

Case 2d: As Case 2a with Grill made of 6x4 waveguides size 79.94x49.12mm

Case 3: Emitter with 2 rows and 4 columns

Waveguide dimensions in emitter:	88.5x181mm with 2mm wall
Input Power:	TE_{03} at 1W and phasing between rows.
Grill:	6x4 waveguide sizes 79.94x49.1 with 6.3mm wall

The best combination is when the coefficients Qt and Qm are the highest while Qd is the lowest (see definitions in table A4). The highest possible Qt is important in order to minimize the amount of reflected power back in the emitter. This power would further be increased if the coupling of the power at the grill is not perfect (for the simulation 100% coupling is assumed). Therefore only cases like 2c, 2d and 3 should be considered.

Results	Case 1	Case 2a	Case 2b	Case 2c	Case 2d	Case 3
Input Power	TE_{02}	TE_{03}	TE_{03}	TE_{03}	TE_{03}	TE_{03}
Ref.Power at emitter in main mode	15 %	11%	38%	9%	10%	11%
Ref. Power in TE_{01}	< 1%	<0.1%	<0.1%	<0.1%	<0.1%	<0.1%
Transmission purity Qm	100%	100%	98%	100%	100%	100%
TE_{06}/TE Forw.	86%	83%	83%	84%	85%	86%
Total TE Ref.	34%	33%	58%	28%	29%	28%
TE_{06}/TE Ref.	28%	45%	58%	28%	26%	27%
Total TM Forw.	4%	4%	8%	3%	2%	2%
Total TM Ref.	4%	4%	9%	3%	2%	2%
Transmission Qt in Grill	85%	88%	61%	91%	90%	89%
Qd in Grill	1.17	1.39	1.72	1.25	1.24	1.18

Qm=Power carried by TE_{06} forward in Hyperguide / Incident Power from emitter

Qt=Power TE_{01} forward in Grill / Incident Power from emitter

Qd=(Pmax-Pmin)/Pmean in Grill

Table A4-1 Results from numerical simulations of the hyperguide.

For all cases the power transmission from the emitter to the hyperguide is total, as Qm=100%. Between 14 and 17% of the total forward TE power in the hyperguide is carried by higher modes, which bounce back and forth inside the cavity. For all cases TE_{08} and TE_{48} modes are excited in the hyperguide (see fig. A4-1).

Very little power is carried by TM modes and they stay in the hyperguide.

Qd is the distribution quality factor inside the grill. When zero, it indicates that the power in each waveguide of the grill is the same. Qd is influenced by wall thickness and the ratio between the number of columns on the grill and the emitter. Using smaller walls at the emitter improves the transmission and Qd, as the results of case 2a and 2c indicate. Qd is further improved if the emitter has the same number of columns as the grill results of case 3 and as 2d indicate.

Results	Case 2d	Case 2d1	Case 2d2
Input Power	TE_{03}	TE_{03}	TE_{03}
Emitter wall thickness (mm)	2	2	0.5
Grill wall thickness (mm)	6.28	2	2
Ref.Power at emitter in main mode	10%	0.5%	0.1%
Ref. Power in TE_{01}	<0.1%	0.05%	0.01%
Transmission purity Qm	100%	100%	100%
TE_{06}/TE Forw.	85%	98%	98%
Total TE Ref.	29%	3%	2%
TE_{06}/TE Ref.	26%	53%	6%
Total TM Forw.	2%	0.1%	0.06%
Total TM Ref.	2%	0.2%	0.09%
Transmission Qt in Grill	90%	100%	100%
Qd in Grill	1.24	0.16	0.16

Table A4-2 Further results from the HYPERCODE simulation.

Case 2a, where mode converters producing TE_{03} mode are used, has a slightly better transmission than case 1 where TE_{02} modes are feeding the hyperguide. However the power inhomogeneity in the grill is higher.

Results for case 2b indicate that only 61% of the incident power is transmitted to a grill of 6x18 waveguides. The distortion in the power distribution inside the grill is also very high as shown in fig. A4-2. For this case around 70% of the area facing the hyperguide is flat metallic walls, which induce a high reflection back inside the hyperguide. For this case the simulation of a transition hyperguide-grill as designed for ITER is not accurate. The present results probably over-estimate the reflection at this interface.

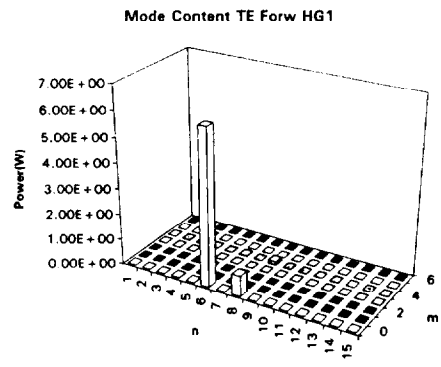

Fig. A4-2 : ITER Hyperguide case 2 (b).

Transmission to a 6x4 waveguide grill improves Qt and Qd compared to case 2a.

A.4.5. Conclusion

For best transmission, a combination of 2x3 emitter with 6x4 grill or 2x4 with 6x4 grill is possible. The later has improved power homogeneity at the grill, but it requires eight vacuum windows instead of six to feed the hyperguide with the same amount of power. Solution 2d is therefore chosen as the best compromise.

With these conditions, around 10% of the incident power is reflected back in the emitter and Qd=1.24. This can probably be improved by using thinner walls at the emitter and tapered walls at the grill, which cannot be modelled with the present Hypercode.

The influence of the wall thickness on the reflected power is indicated in the following table where case 2d is compared with 2 cases where only the wall thickness at the grill for case 2d1 and both at the grill an the emitter for case 2d2 have been reduced. In these conditions total power transmission is achieved and the good power homogeneity inside the grill will also provide an optimized launched power spectrum.

APPENDIX 5
RECTANGULAR POLOIDAL MODE CONVERTER

A.5.1. Principle

The shape of the H plane is formed of sinusoïds which have a geometric wavenumber which is the beating wavelength between the wavenumber of the mode at the input to the one at the output. The amplitude of the geometrical wave and the number of waves are adjusted in such a way to realize a certain conversion efficiency.

The computation of the forward and backward propagating modes is done using the telegraphist equation which is derived from Maxwell equations. It is a linear first order differential equation in longitudinal coordinate which links all the forward and backward waves of propagating modes by coupling coefficients. The considered modes are the TE_{0n} modes since the E plane size is unchanged. For each position the energy conservation is checked.

A.5.2. Application to Tore Supra

a) Calculation of the mode converter parameters

Since the working frequency is 3.7GHz and that a feeder with the TE_{03} mode was necessary, a TE_{01} to TE_{03} mode converter has been computed and then realized.

For the calculation the TE_{01} to the TE_{04} modes have been considered. Since the mode converter is symmetric the coupling coefficients between odd and even modes are null. That also means that if the mode converter is well matched, only odd modes are excited.

The forward and the backward power amplitude of the 2 odd modes is given in (Fig A5-1). The initial conditions are that only the forward wave amplitude of the TE_{01} mode is supposed not null at the input. The computed conversion efficiency from the TE_{01} to the TE_{03} mode is 98.7 %.

The geometrical sizes of the mode converter are :

- a total length of 791mm with 3.5 periodic waves.
- the E plane size is 40mm.
- the H plane size is oscillating from 130mm to 192mm.

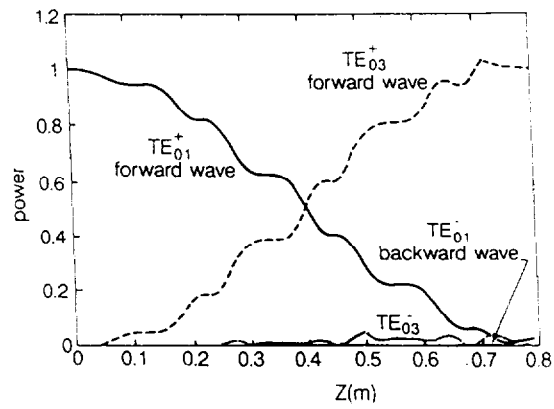

Fig. A5-1 : Power in forward and backward waves for TE_{01} and TE_{03} mode versus the propagating length inside the mode converter.

b) Measurement of the mode converter characteristics.

Such a mode converter has been realized in copper for lower RF level tests. The conversion efficiency was measured and checked using 2 techniques :

- the first one is with electric probes measuring the total electric field in the transverse H direction at 2 different positions in the longitudinal direction (see for example at the mode converter output, Fig. A5-2). The amplitude and the phase of the propagating modes have then been determined. An experimental conversion efficiency of 99 % has been found. That is verified by observing the ratio of the central peak to the lateral one in the total electric field shape (Fig. A5-3) at the output of the mode converter in a constant size oversized waveguide where it is shown that it changes from 0.9 to 1.1. That is in total agreement with the conversion efficiency which means that there is an electric field amplitude of 99 % of TE_{03} mode for 10% of TE_{01} mode.

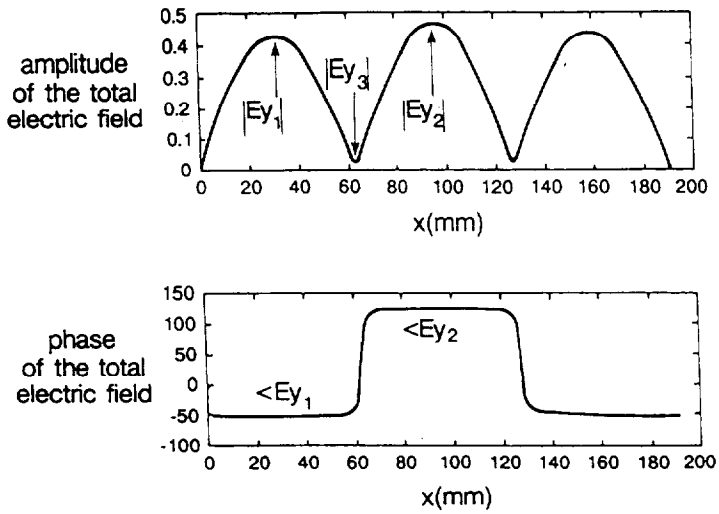

Fig. A5-2 : Amplitude and phase of the total electric field.

The phase shift between the central peak and the lateral one is as expected of 180 degrees all along the longitudinal direction of propagation.

- the second one is by measuring the power division ratio at the output of a 3 waveguides poloidal junction set at the mode converter output. There the division ratio has been measured to be 33 %, 36 %, 33 %. These numbers are in total agreement with the square of the ratio defined in (Fig. A5-3) at the output of the mode converter. The distance between the mode converter output and this 3 waveguides poloidal junction has been changed and the measurement made with the first method have been confirmed.

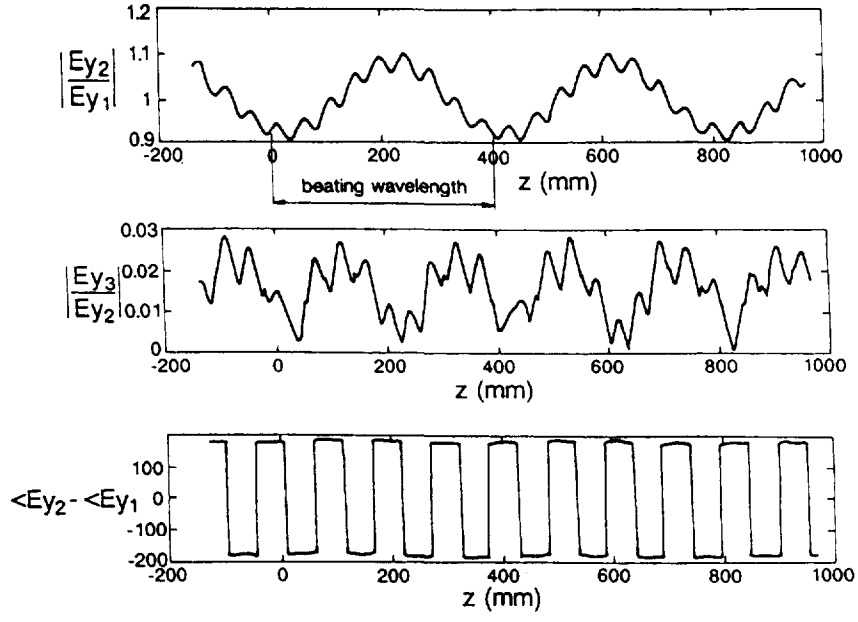

Fig. A5-3 : Ratio of electric field between central and lateral row.

c) Stability of the mode converter with respect to reflected waves

Since the numerical code has been validated by the previous measurements the effect of a backward wave for a TE_{01} mode or TE_{03} mode at the mode converter input has been studied.

For the TE_{01} mode the effect is shown on (Fig. A5-4 and A5-5). It is observed in the first figure that the backward wave amplitude of theTE_{03} mode at the output increases to a value which is higher than the reflection coefficient of the TE_{01} mode at the input. That is explained by the conversion efficiency which is not 100% meaning that when TE_{03} mode is reflected at the output, one part stays in this mode and is reflected back again, explaining then the increase of amplitude of the TE_{03} mode forward amplitude at the output. In the second figure the amplitude at the output of the forward and backward wave of the TE_{01} mode changes slowly.

For the TE_{03} mode the effect is shown on (Fig. A5-6 and A5-7). In the first one the amplitude of the TE_{01} mode backward wave is a little lower than the reflection coefficient of the TE_{03} mode at the input. That leads therefore to a small change of the TE_{03} mode forward amplitude at the output of the mode converter. In the second one at the mode converter output the amplitude of the backward wave of the TE_{03} mode at the output and of the forward wave of the TE_{01} mode slowly increase.

In these two cases the proportion of the TE_{03} mode forward wave is not too affected if the power reflection coefficient at the mode converter output for the 2 modes is less than 10 %. This can be realized using the self-matching properties of multijunctions

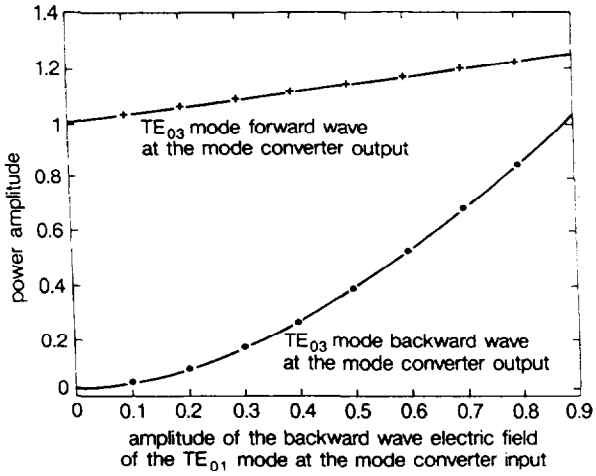

Fig. A5-4 : Power Amplitude of the TE_{03} mode forward and backward wave at the mode converter output versus the electric field backward wave amplitude of the TE_{01} mode at the mode convertor input.

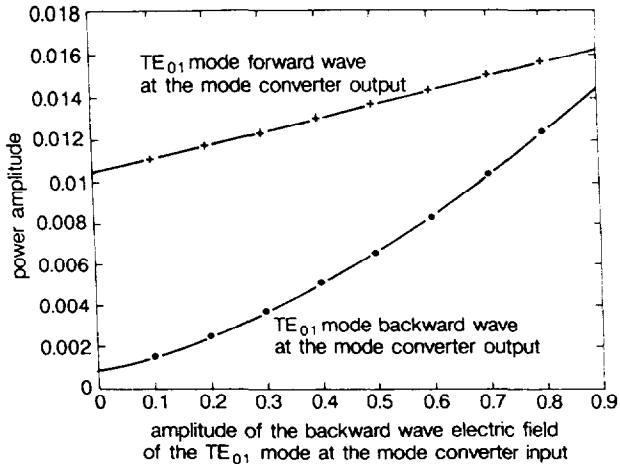

Fig. A5-5 : Power amplitude of the TE_{01} mode forward and backward wave at the mode converter output versus the electric field backward wave amplitude of the TE_{01} mode at the mode converter input.

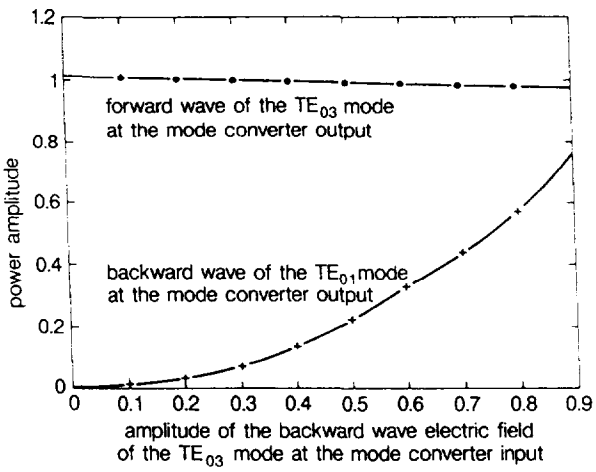

Fig. A5-6 : Power amplitude of the TE_{01} mode backward wave and TE_{03} mode forward wave at the mode converter output versus the electric field amplitude of the TE_{03} mode backward wave at the mode converter input.

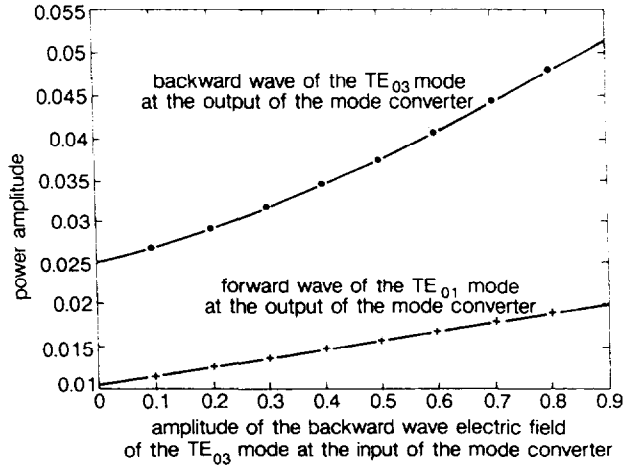

Fig. A5-7 : Power amplitude of the TE_{01} mode forward wave and TE_{03} mode backward wave at the mode converter output versus the electric field amplitude of the TE_{03} mode backward at the mode converter input.

First RF low level experiments have been done with the mode converter assembled with a 3-waveguide poloidal junction. The main results is that if the symmetry is respected by setting the same bad loads on symmetric output ports the dividing ratio and the phase shift of 180

degrees between the central output waveguide and the lateral ones is respected. That is no more true in other case.

For ITER the mode converter would be designed using the same principle.

REFERENCES

[1] W.M. Nevins, et al., to appear in proceedings of the 15th Int. Conf. on Plasma Phys. and Contr. Nuclear Fusion, Seville (Spain), 1994.

[2] C. Gormezano, et al., 14th Int. Conf. on Plasma Phys. and Contr. Nuclear Fusion, Würzburg, Vol. 1, p. 587 (1992).

[3] F.X. Söldner, et al., to appear in proceedings of the 21st Eur. Conf. on Controlled Fusion and Plasma Physics, Montpellier (France), 1994.

[4] G.V. Pereverzev, Nucl. Fusion **32** (1992) 1091.

[5] G.V. Pereverzev, et al., Nucl. Fusion **32** (1992) 1023.

[6] V.V. Parail, et al., internal report JET-P(93) 87, to be published.

[7] M.R. O'Brien, et al., Proc. IAEA Tech. Committee Meeting on Advances in Simulation and Modelling of Thermonuclear Plasmas, p. 527, Montreal (1992).

[8] E. Ott, Phys. Fluids **22** (1979) 1732.

[9] C.F.F. Karney, N.J. Fisch, Phys. Fluids **22** (1979) 1817.

[10] V. Fuchs, R.A. Cairns, M.M. Shoucri, K. Hizanidis, A. Bers, Phys. Fluids **28** (1985) 3619.

[11] Y.F. Baranov et al., 20th Eur. Conf. on Controlled Fusion and Plasma Physics, Vol.III, p. 881, Lisbon, 1993.

[12] G.V. Pereverzev, et al., 'ASTRA - An Automatic System for Transport Analysis in a Tokamak', IPP report, 5/42, Aug. 1991.

[13] J.G. Wegrowe and G.W. Pacher, to appear in proceedings of the 21st Eur. Conf. on Controlled Fusion and Plasma Physics, Montpellier (France) 1994.

[14] X. Litaudon, D. Moreau, et al., report EUR-CEA-FC-1472, Centre d'Etudes de Cadarache (1992).

[15] C.B. Forrest, K. Kupfer, et al., General Atomics report GA-A21680 (1994), submitted to Phys. Rev. Lett. (1994).

[16] Ph. Bibet, X. Litaudon and D. Moreau, Proc. of the IAEA Tech Committee Meeting on RF Launchers for Plasma Heating and Current Drive, November 1993, Naka (Japan).

[17] A.S. Kaye, 'Progress in ICRH and Lower Hybrid Launcher Development', Plasma Phys. and Control. Fusion **35** (1992) A71-90 .

[18] G. Tonon, ITER Report ITER-IL-HD-5-9-E-2 (1989).

[19] J.G. Van der Laan, 'Prediction for Disruption Erosion of ITER PFC'; A Comparison of Experimental and Numerical Results, paper 148 at ISFNT-2, Karlsruhe (1991).

[20] Ph. Bibet and T.K. NGuyen, 'Design of a new antenna for LHCD on Tore Supra', Proc. of the IAEA Tech Committee Meeting on RF Launchers for Plasma Heating and Current Drive, November 1993, Naka (Japan).

[21] Ph. Bibet and T.K. NGuyen, 'Experimental and Theoretical Results concerning the development of the main RF components for the next Tore Supra LHCD antenna', Symposium on Fusion Technology, Karlsruhe (1994).

[22] Y. Ikeda, et al., 'Development and operation of JT-60 LHRF launchers',Plasma Devices and Operation, **1**,155 (1991). ITER Technical Meeting on Radiation Effects on In-vessel Components, Garching, Nov.1993.

[23] G. Rey, M. Goniche, et al, 'High Power and Long Pulse Capability of LHCD System on Tore Supra', Proc. 17 th Symposium on Fusion Technology, Rome (1992).

[24] G. Rey, M. Goniche, et al, 'High Power and Long Pulse Capability of the LH System on Tore Supra and Testbed Facility'. AIP Conference on Radiofrequency Power in Plasmas, 10 th Topical Conference, Boston (1993).

[25] F. Leuterer, et al., Coupling of the 2x24 Waveguide Grill for Lower Hybrid Waves in ASDEX, Plasma Physics and Contr. Fusion **33**, 169 (1991).

[26] K. Ushigusa, et al., Paper E-III-1, 12th Int. Conf. Plasma Physics on Contr. Nucl. Fusion Research, Nice (1988).

[27] X Litaudon et al., Lower Hybrid Wave Coupling in Tore Supra through Multijunction Launchers, Nucl. Fusion, **32** (1992) 1883.

[28] J.E. Stevens, et al, Nuclear Fusion **28** (1988) 217.